University of Montana

ScholarWorks at University of Montana

2013

Recent climate and fire disturbance impacts on boreal and arctic ecosystem productivity estimated using a satellite-based terrestrial carbon flux model

Yonghong Yi
University of Montana - Missoula

John S. Kimball
University of Montana - Missoula

Lucas A. Jones

Rolf H. Reichle
NASA

Ramakrishna R. Nemani

See next page for additional authors

Follow this and additional works at: https://scholarworks.umt.edu/ntsg_pubs

Let us know how access to this document benefits you.

Recommended Citation

Yi, Y., J. S. Kimball, L. A. Jones, R. H. Reichle, R. Nemani, and H. A. Margolis (2013), Recent climate and fire disturbance impacts on boreal and arctic ecosystem productivity estimated using a satellite-based terrestrial carbon flux model, J. Geophys. Res. Biogeosci., 118, 606–622, doi:10.1002/jgrg.20053

Authors

Yonghong Yi, John S. Kimball, Lucas A. Jones, Rolf H. Reichle, Ramakrishna R. Nemani, and Hank A. Margolis

Recent climate and fire disturbance impacts on boreal and arctic ecosystem productivity estimated using a satellite-based terrestrial carbon flux model

Yonghong Yi,[1,2] John S. Kimball,[1,2] Lucas A. Jones,[1,2] Rolf H. Reichle,[3] Ramakrishna Nemani,[4] and Hank A. Margolis[5]

[1] Warming and changing fire regimes in the northern ($\geq$45°N) latitudes have consequences for land-atmosphere carbon feedbacks to climate change. A terrestrial carbon flux model integrating satellite Normalized Difference Vegetation Index and burned area records with global meteorology data was used to quantify daily vegetation gross primary productivity (GPP) and net ecosystem CO_2 exchange (NEE) over a pan-boreal/Arctic domain and their sensitivity to climate variability, drought, and fire from 2000 to 2010. Model validation against regional tower carbon flux measurements showed overall good agreement for GPP (47 sites: R = 0.83, root mean square difference (RMSD) = 1.93 g C m^{-2} d^{-1}) and consistency for NEE (22 sites: R = 0.56, RMSD = 1.46 g C m^{-2} d^{-1}). The model simulations also tracked post-fire NEE recovery indicated from three boreal tower fire chronosequence networks but with larger model uncertainty during early succession. Annual GPP was significantly (p < 0.005) larger in warmer years than in colder years, except for Eurasian boreal forest, which showed greater drought sensitivity due to characteristic warmer, drier growing seasons relative to other areas. The NEE response to climate variability and fire was mitigated by compensating changes in GPP and respiration, though NEE carbon losses were generally observed in areas with severe drought or burning. Drought and temperature variations also had larger regional impacts on GPP and NEE than fire during the study period, though fire disturbances were heterogeneous, with larger impacts on carbon fluxes for some areas and years. These results are being used to inform development of similar operational carbon products for the NASA Soil Moisture Active Passive (SMAP) mission.

1. Introduction

[2] Northern boreal and arctic ecosystems are purported to be a considerable land sink for atmospheric CO_2 [*Euskirchen et al.*, 2006; *McGuire et al.*, 2009], though sensitivity of the regional carbon cycle to a warming climate is uncertain [*McGuire et al.*, 2009; *Hayes et al.*, 2011]. The high latitudes have experienced generally greater warming than other global areas in recent decades [*Serreze and Francis*, 2006]. A lengthening growing season has been linked to vegetation greening and enhanced productivity in the northern latitudes [e.g., *Nemani et al.*, 2003; *Chen et al.*, 2006; *Beck and Goetz*, 2011]. However, increasing vegetation water stress and enhanced autumn respiration may be offsetting the potential benefits of longer growing seasons and decreasing regional carbon sequestration [*Angert et al.*, 2005; *Piao et al.*, 2008; *Zhang et al.*, 2008]. Boreal forests have had more frequent and widespread wildfire and insect disturbances [*Bond-Lamberty et al.*, 2007; *Kurz et al.*, 2008], which may alter vegetation composition and function and associated growth and respiration processes [*Amiro et al.*, 2010; *Coursolle et al.*, 2012]. Moreover, a large portion of soil organic carbon stored in northern boreal forest and tundra areas is potentially vulnerable to soil warming and likely more frequent burning due to climate warming [*Turetsky et al.*, 2010; *Mack et al.*, 2011].

[3] A diverse response of northern ecosystems to regional warming and drought has been reported from limited field experiments [e.g., *Chen et al.*, 2006; *Welp et al.*, 2007;

[1]Flathead Lake Biological Station, The University of Montana, Polson, Montana, USA.
[2]Numerical Terradynamic Simulation Group, The University of Montana, Missoula, Montana, USA.
[3]Global Modeling and Assimilation Office, NASA Goddard Space Flight Center, Greenbelt, Maryland, USA.
[4]NASA Ames Research Center, Moffett Field, California, USA.
[5]Centre d'étude de la forêt, Faculté de foresterie, géographie et de géomatique, Université Laval, Québec, Québec, Canada.

Corresponding author: Y. Yi, Flathead Lake Biological Station, The University of Montana, Polson MT 59860, USA. (yonghong.yi@ntsg.umt.edu)

Schwalm et al., 2010; *Yi et al.*, 2010b; *Peng et al.*, 2011], while extension of these findings to the larger pan-boreal/ Arctic region is constrained by the limited extent of these studies and a sparse regional measurement network. A recent decline in northern ecosystem productivity, especially in the boreal forest, has been reported from satellite measurement records [e.g., *Angert et al.*, 2005; *Goetz et al.*, 2007; *Beck and Goetz*, 2011]. However, many of these studies are based on satellite-derived vegetation "greenness" indices (VIs) including the EVI (Enhanced Vegetation Index) and NDVI (Normalized Difference Vegetation Index) that do not distinguish underlying gross primary productivity (GPP) and respiration processes or their environmental drivers. Meanwhile, the impact of wildfire on the northern carbon cycle is increasing, while the associated effects on regional vegetation and soil carbon recovery have not been investigated using ecosystem models until recently [*Balshi et al.*, 2007; *Yi et al.*, 2010a]. Therefore, regional applications of ecosystem models are desirable to clarify recent impacts from climate variability and disturbance on the northern carbon cycle.

[4] Satellite remote sensing offers a diverse set of land parameter retrievals that can serve as critical inputs to regional ecosystem models for estimating land-atmosphere carbon fluxes and associated climate impacts to the terrestrial carbon budget [e.g., *Nemani et al.*, 2003; *Potter et al.*, 2003; *Zhang et al.*, 2008; *Kimball et al.*, 2009]. The Moderate Resolution Imaging Spectroradiometer (MODIS) provides continuous, well calibrated, and relatively long-term global records that are sensitive to photosynthetic canopy cover [*Running et al.*, 2004]; global monitoring from these sensors can also detect abrupt disturbance-related vegetation changes [*Mildrexler et al.*, 2007; *Giglio et al.*, 2010]. Satellite microwave sensors provide synergistic information on land surface moisture and temperature variations owing to strong microwave sensitivity to associated changes in land surface dielectric properties and emissivity [*Ulaby et al.*, 1982]. Land surface retrievals at longer microwave wavelengths also have reduced sensitivity to solar illumination effects, clouds, and atmospheric aerosol contamination relative to optical sensors; these properties have been exploited for determining daily landscape freeze/thaw (FT) status and nonfrozen season variability, which provides an effective surrogate for frozen temperature constraints to vegetation productivity and the potential growing season in boreal/Arctic regions [*Kimball et al.*, 2004; *Kim et al.*, 2012]. The planned NASA Soil Moisture Active Passive (SMAP) mission will provide global measurements of surface soil moisture and FT status, with improved spatial resolution (<10 km) and enhanced L-band microwave sensitivity to soil processes relative to current satellite microwave sensors [*Entekhabi et al.*, 2010]. The SMAP land parameter retrievals will inform higher level land model simulations including a planned level 4 carbon (L4_C) product that will provide regular global estimates of terrestrial carbon fluxes and underlying environmental drivers [*Kimball et al.*, 2012]. These new measurements and geophysical products are intended to improve understanding of processes linking terrestrial water, energy, and carbon cycles, quantify the net carbon flux in boreal landscapes, and reduce uncertainties regarding the purported missing carbon sink on land [*Entekhabi et al.*, 2010].

[5] In this study, we applied a terrestrial carbon flux (TCF) model partially driven by satellite-derived FPAR (Fraction of Photosynthetically Active Radiation absorbed by vegetation), FT, and burned area inputs to estimate daily GPP, net ecosystem CO$_2$ exchange (NEE), and surface (<10 cm depth) soil organic carbon (SOC) stocks over all northern vegetated land areas. The TCF model used for this study is similar to the L4_C algorithm being developed for the SMAP mission. Our primary objectives were to use the TCF projections to examine how recent climate variability and fire disturbance have affected northern GPP and NEE carbon sink activity during the 11 year satellite record (2000–2010). We hypothesized that potential productivity gains from regional warming still outweigh productivity losses caused by recent drought stress and wildfire disturbance in the northern latitudes, while prediction of NEE is more uncertain due to similar, compensating GPP and ecosystem respiration (R_{eco}) responses to these factors. These results were also used to test the initial algorithm and model performance for the planned SMAP L4_C product.

[6] The following sections include descriptions of the TCF model equations and methods used for the model simulations, validation and uncertainty assessment (section 2); presentation of model validation results relative to independent GPP and NEE estimates from northern tower eddy covariance CO$_2$ flux measurement sites and SOC data from soil inventory records (section 3.1); model assessment of regional drought and fire impacts on the northern carbon cycle (section 3.2); discussion of model and observation uncertainties (section 4); and the implications of the study results for informing development of similar carbon model simulations for the SMAP mission (section 5).

2. Methods

[7] This study extends a previous TCF model development effort that used satellite [Advanced Microwave Scanning Radiometer-EOS (AMSR-E)] microwave soil moisture and temperature retrievals, and MODIS-derived GPP inputs within a three-pool soil decomposition model to estimate NEE over a regional network of northern temperate grassland, boreal forest, and tundra tower sites [*Kimball et al.*, 2009]. A light use efficiency (LUE) algorithm [*Running et al.*, 2004] and the soil decomposition model were combined in this study to estimate surface SOC stocks and carbon fluxes under dynamic steady state conditions during the study period. A synthetic approach integrating information from fire chronosequence tower carbon flux observations, satellite VIs (NDVI, EVI), and burned area products was also used to account for nonsteady state post-fire recovery effects on the TCF calculations. The following sections describe the model equations (section 2.1), primary data sets used for model inputs and validation (section 2.2), the model parameterization scheme (section 2.3), and a Monte Carlo based model uncertainty assessment (section 2.4).

2.1. Model Description

2.1.1. TCF Equations

[8] NEE (g C m^{-2} d^{-1}) is computed on a daily basis as the residual difference between GPP and R_{eco} defined as the sum of autotrophic (R_a) and heterotrophic (R_h) components:

$$\text{NEE} = (R_a + R_h) - \text{GPP} \qquad (1)$$

where positive (+) and negative (−) NEE fluxes denote the terrestrial loss or uptake of CO$_2$, respectively. A LUE

approach similar to the MODIS (MOD17) productivity algorithm [*Running et al.*, 2004] was used to estimate GPP:

$$GPP = \varepsilon \times FPAR \times PAR \qquad (2)$$

where ε (g C MJ^{-1}) is the LUE coefficient converting absorbed photosynthetically active solar radiation (APAR, MJ m^{-2} d^{-1}) to vegetation biomass and FPAR defines the fraction of incident PAR (MJ m^{-2} d^{-1}) absorbed by the vegetation canopy. PAR is estimated as a constant proportion (0.45) of incident shortwave solar radiation at the surface, which is derived from reanalysis data. The LUE coefficient ε is derived from a maximum LUE coefficient (ε_{mx}, g C MJ^{-1}) prescribed for each land cover class and reduced for suboptimal environmental conditions:

$$\varepsilon = \varepsilon_{mx} \times T_{mn\_scalar} \times VPD_{scalar} \times FT_{scalar} \qquad (3)$$

where T_{mn_scalar} and VPD_{scalar} are dimensionless rate scalars for sub-optimal temperature and moisture conditions represented by respective daily minimum air temperature and atmospheric vapor pressure deficit inputs. These rate scalars are defined as simple linear ramp functions [*Heinsch et al.*, 2006] and vary according to prescribed minimum and maximum environmental constraints defined for different global biome types (T_{mn_min} and T_{mn_max}, VPD$_{min}$ and VPD$_{max}$, Table 1). An additional FT$_{scalar}$ term defines the frozen temperature constraints to landscape water mobility and GPP as determined from regional comparisons between tower observation based GPP and daily FT retrievals from satellite microwave remote sensing [*Kimball et al.*, 2004; *Kim et al.*, 2012]. In this study, FT$_{scalar}$ is set to 0 (fully constrained) if the FT retrievals indicate frozen landscape conditions, 1 (no constraint) under nonfrozen conditions, and 0.5 (partially constrained) for transitional FT days defined by midday thawing and nighttime freezing.

[9] The R_a term (g C m^{-2} d^{-1}) in equation (1) represents the sum of vegetation growth and maintenance respiration and is estimated as a fixed proportion of GPP for each biome type based on an assumption of conservatism in vegetation carbon use efficiency (CUE) within similar plant functional types [*Waring et al.*, 1998; *Gifford*, 2003] as follows:

$$R_a = (1 - CUE) \times GPP \qquad (4)$$

where CUE is the dimensionless ratio of vegetation net primary production (NPP) to GPP, and NPP (g C m^{-2} d^{-1}) represents the difference between GPP and R_a. While the assumption of CUE conservatism provides a key simplification for a remote sensing based algorithm, the proportion of plant photosynthesis devoted to biophysical growth and maintenance may vary under changing environmental conditions and over the course of vegetation development [*DeLucia et al.*, 2007].

[10] The R_h term (g C m^{-2} d^{-1}) in equation (1) is computed as the sum of variable soil decomposition and respiration rates from three distinct carbon pools as follows:

$$R_h = K_{met}C_{met} + (1 - F_{str}) \times K_{str}C_{str} + K_{rec}C_{rec} \qquad (5)$$

where C_{met}, C_{str}, and C_{rec} represent metabolic, structural, and recalcitrant SOC pools (g C m^{-2}), respectively, and K_{met}, K_{str}, and K_{rec} are the corresponding decomposition rate parameters (day^{-1}). The metabolic and structural SOC pools represent plant litter with relatively short (e.g., ≤5 years)

turnover periods, while the recalcitrant or slow pool represents more physically and chemically protected SOC with a longer turnover time. In *Kimball et al.* [2009], a fixed proportion of carbon from the structural SOC pool was transferred to the recalcitrant pool, which was found to be effective at annual time scales. In this study, we assume that a fixed proportion (F_{str}) of the respiration flux from the structural pool is transferred to the slow pool on a daily basis:

$$dC_{met}/dt = C_{fract}NPP - K_{met}C_{met} \qquad (6)$$

$$dC_{str}/dt = (1 - C_{fract})NPP - K_{str}C_{str} \qquad (7)$$

$$dC_{rec}/dt = F_{str}K_{str}C_{str} - K_{rec}C_{rec} \qquad (8)$$

where the C_{fract} term defines the rate in which litterfall from NPP is allocated to C_{met} and varies for different biome types and associated litterfall chemistry [*Ise and Moorcroft*, 2006]. Estimated annual litterfall is evenly distributed on a daily basis over each annual cycle for all biome types. This finer daily temporal allocation of litterfall allows for better representation of the seasonal dynamics of the two fast SOC pools, which generally have faster (<1 year) turnover rates, especially under warmer conditions. This approach ignores the characteristic variable litterfall seasonality in deciduous ecosystems but facilitates regional application by avoiding more complex canopy phenology representation, model parameterization and input requirements, and associated uncertainty [*White et al.*, 2000].

[11] The soil decomposition rate is derived as the product of a theoretical maximum rate constant (K_{mx}, 0.0301 day^{-1}) [*Ise and Moorcroft*, 2006] and dimensionless multipliers for soil temperature (T_{mult}) and moisture (W_{mult}) constraints to decomposition under prevailing climate conditions:

$$K_{met} = K_{mx} \times T_{mult} \times W_{mult} \qquad (9)$$

where T_{mult} and W_{mult} vary between 0 (fully constrained) and 1 (no constraint). The decomposition rate parameters for C_{str} and C_{rec}, i.e., K_{str} and K_{rec}, are estimated as 40% and 1% of K_{met} [*Ise and Moorcroft*, 2006]. The soil decomposition rate response to temperature follows an Arrhenius type function [*Lloyd and Taylor*, 1994]:

$$T_{mult} = \exp\left\{308.56\left[1/(T_{opt} + 46.02) - 1/(T_s + 46.02)\right]\right\} \qquad (10)$$

where T_{opt} and T_s are the respective reference and input surface soil temperatures (°C) for $T_s \le T_{opt}$. Above the reference temperature (T_{opt}), soil decomposition is no longer limited by temperature; under these conditions, soil moisture is expected to decline with warmer soil temperatures and becomes the primary constraint to decomposition.

[12] The soil decomposition and R_h response to soil moisture varies according to multiple factors including soil texture, climate, and vegetation type but generally has optimum rates at intermediate soil moisture levels and is increasingly inhibited at lower or higher soil water contents according to site observations and laboratory incubation studies [*Davidson et al.*, 2000]. For this investigation, the soil moisture constraint on soil decomposition under unsaturated conditions (SM < SM$_{opt}$) is defined as follows:

$$W_{mult} = \left[1 + a\exp(b \times SM_{opt})\right]/\left[1 + a\exp(b \times SM)\right] \qquad (11)$$

where a and b are empirical fitting parameters that define the decomposition rate response to soil moisture variability and

Table 1. General Biome Properties Look-Up Table (BPLUT) Describing Ecophysiological Parameters for TCF Simulations of Northern Land Cover Types[a]

Parameters	ENF	DNF	DBF	MF	SRB	GRS	CRP
			LUE model parameters				
ε_{mx} (g C MJ^{-1})	1.05	1.15	1.20	1.07	0.85	0.85	1.06
T_{mn_min} (°C)	−8.0	−8.0	−6.0	−7.0	−8.0	−8.0	−8.0
T_{mn_max} (°C)	8.3	10.4	9.9	9.5	8.8	12.0	12.0
VPD$_{min}$ (pa)	500	500	500	500	500	752	500
VPD$_{max}$ (pa)	4000	4160	4160	2732	4455	5500	5071
CUE	0.55	0.55	0.55	0.50	0.60	0.60	0.55
			Soil decomposition model parameters				
C_{fract}	0.49	0.67	0.67	0.59	0.62	0.76	0.78
F_{str}	0.7	0.7	0.7	0.7	0.7	0.7	0.7
T_{opt} (°C)	25	25	25	25	25	25	25
SM$_{opt}$	0.6	0.6	0.6	0.6	0.6	0.6	0.6
a	9.9	9.9	9.9	9.9	9.9	9.9	9.9
b	−6.13	−6.13	−6.13	−6.13	−6.13	−6.13	−6.13

[a]Note: ENF: evergreen needleleaf forest; DBF: deciduous broadleaf forest; DNF: deciduous needleleaf forest; MF: mixed forest; SRB: shrubland; GRS: grassland; CRP: cropland.

may vary in different climate regimes. SM is expressed as a proportion (%) of saturation, and SM$_{opt}$ is the optimal soil moisture level (%) below which R_h is constrained by drier soil conditions. There is no moisture constraint (i.e., $W_{mult} = 1$) to R_h where SM ≥ SM$_{opt}$, based on the assumption that most land areas are not saturated long enough to deplete soil oxygen and constrain R_h at the relatively coarse (0.5°) scale of the model simulations. This is also consistent with previous studies indicating wetland adaptations to wet soil conditions and a general lack of landscape level observational evidence for extended SM saturation and associated reductions in aerobic decomposition [e.g., *Chimner*, 2004].

2.1.2. Fire Disturbance and Vegetation Recovery Impacts

[13] To represent the redistribution of dead plant material and SOC consumption following fire disturbance, a portion (η_1) of NPP was added to C_{met} and C_{str}, and a fixed portion ($1 - \eta_2$) of SOC was removed from C_{rec} as follows:

$$C_{met} = C_{met0} \times (1 - BF) + BF \times \eta_1 \times NPP \times C_{fract} \quad (12)$$

$$C_{str} = C_{str0} \times (1 - BF) + BF \times \eta_1 \times NPP \times (1 - C_{fract}) \quad (13)$$

$$C_{rec} = C_{rec0} \times (1 - BF) + BF \times \eta_2 \times C_{rec0} \quad (14)$$

where a spatial burned area fraction term (BF) ranging from 0 (no burning) to 1 (complete burning), was used to account for the effects of incomplete burning on the redistribution of fire detritus and SOC removal and was derived from ancillary inputs (section 2.2.2). C_{met0}, C_{str0}, and C_{rec0} represent the three carbon pools (g C m^{-2}) prior to burning, which can be approximated by steady state carbon pools for the boreal region with a general fire return interval of more than 50 years [*Balshi et al.*, 2007]. The η_1 term represents the add-in proportion of detritus to the two fast pools, and $1 - \eta_2$ is the proportion of prefire SOC lost to combustion depending on the fire severity and local soil carbon characteristics (section 2.3). The η_1 parameter was used to simulate the R_h pulse from decomposition of additional dead plant material following fire disturbance, and may not effectively represent variable decomposition of coarse woody debris. The redistribution of dead plant material (equations (12) and (13)) is also relatively simple because the TCF model does not simulate aboveground biomass; this differs from

more detailed treatment of disturbance in other process models that account for redistribution of different plant components, including leaves, fine roots, and coarse woody debris [e.g., *Thornton et al.*, 2002]. However, a general correlation between total ecosystem live biomass and GPP under steady state conditions [*Law et al.*, 2003] supports the assumption that detritus added to the two fast SOC pools is proportional to steady state ecosystem productivity.

2.2. Data Sets
2.2.1. Eddy Covariance Flux Data

[14] Tower measurements of carbon fluxes from 47 predominantly undisturbed northern sites (Figure 1a) within the modeling domain were obtained from the La Thuile 2007 synthesis of global FLUXNET observations [*Baldocchi*, 2008] and used for independent validation of TCF steady state GPP and NEE simulations. The tower daily carbon flux estimates are derived from half-hourly eddy covariance CO$_2$ flux measurements that have been processed and aggregated using consistent gap filling and quality control procedures [*Reichstein et al.*, 2005]. Other La Thuile tower carbon flux estimates representing selected biomes independent from the validation sites were used for model calibration (section 2.3). The TCF simulations were conducted for individual tower sites at 1 km spatial resolution consistent with MODIS (MOD12) land cover classification inputs within 3 × 3 grid cell (9 km^2) windows centered over each tower location; only sites with the same local land cover as the dominant land cover class of the overlying 3 × 3 km modeling window were selected for model calibration and validation. The resulting tower sites represent the predominant biome types within the northern domain, including evergreen needleleaf forest (ENF), deciduous needleleaf forest (DNF), deciduous broadleaf forest (DBF), mixed forest (MF), shrublands, grasslands, and croplands.

[15] Tower measurements from three groups of fire chronosequence sites (≥45°N, Table 2) were used within the TCF framework following equations (12)–(14) to account for post-fire vegetation productivity and SOC recovery; the model simulations for each chronosequence assumed complete burning (BF = 1) from the initial fire disturbance. The three boreal forest site networks are located in Manitoba (MB) [*Goulden et al.*, 2011] and Saskatchewan
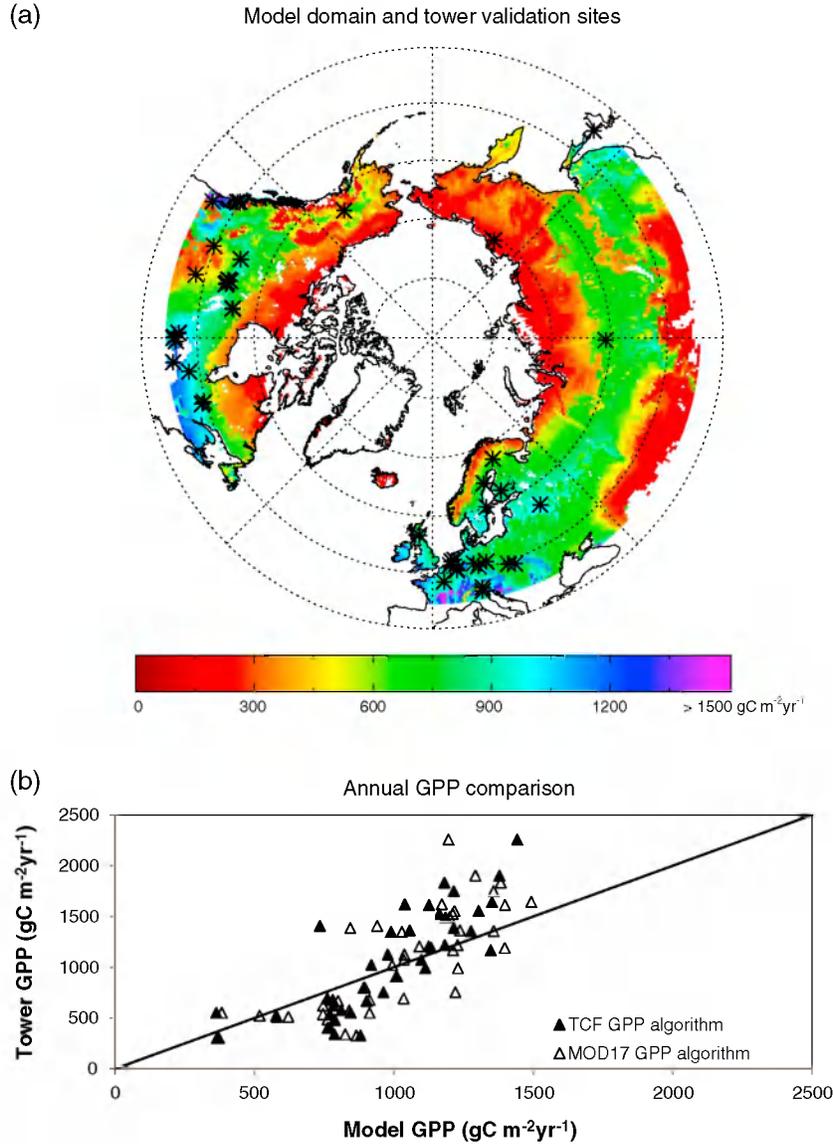
(a)   Model domain and tower validation sites

(b)   Annual GPP comparison

Figure 1. (a) Model domain and location of tower sites ($\geq45°$N) used for algorithm validation and overlain on the TCF LUE model derived multiyear average annual GPP (2000–2010, $g\,C\,m^{-2}\,yr^{-1}$); (b) comparison between modeled (TCF and MOD17) and observed annual GPP at the 42 northern tower sites, including 27 ENF, 4 DBF, 8 MF, and 3 grassland sites. Average RMSD values of modeled daily GPP fluxes versus the tower observations are $1.95\,g\,C\,m^{-2}\,d^{-1}$ (TCF) and $2.10\,g\,C\,m^{-2}\,d^{-1}$ (MOD17); average R values are 0.84 (TCF) and 0.81 (MOD17).

(SK) [*Mkhabela et al.*, 2009] Canada, and Alaska (AK) [*Welp et al.*, 2007]. The MB and AK sites are largely dominated by black spruce, while mixed components of black spruce, jack pine, and trembling aspen occur at the southern SK sites [*Amiro et al.*, 2010]. Although care was taken in locating the sites in similar environmental conditions within each chronosequence, variability may still exist among sites due to differences in local environmental factors such as soil type and local hydrology.

2.2.2. Model Driving Data

[16] Primary TCF environmental drivers for this study included daily surface meteorology, soil moisture, and soil temperature inputs from global model reanalysis and satellite-based 16 day NDVI and daily FT records. Daily surface (2 m height) minimum air temperature, atmosphere

vapor pressure deficit (VPD), downward shortwave solar radiation, and surface soil temperature (≤10 cm) and soil moisture (≤2 cm) were aggregated from hourly surface fields of the Modern-Era Retrospective analysis for Research and Applications (MERRA) reanalysis [*Yi et al.*, 2011]; MERRA is based on the GEOS-5 land model and is similar to the modeling and data assimilation framework that will provide surface meteorology, soil moisture, and soil temperature inputs for planned SMAP L4_C model calculations [*Kimball et al.*, 2012]. MODIS NDVI (MOD13A2) global 1 km resolution, 16 day composite time series were temporally interpolated to a daily time step and used to estimate FPAR using global biome-specific empirical relationships (R > 0.75, p < 0.001) established between best quality (indicated by MODIS QC metadata) retrievals from 1 year (2005) of

Table 2. List of Fire Chronosequence Tower Sites (≥45°N) Used for the TCF Disturbance Analysis[a]

Chronosequence	Site Name	Location	Biome Type	Year of Most Recent Disturbance	Annual T_{air} (°C)	Annual P (mm)	References
Manitoba (MB)	CA-NS1	55.879°N 98.484°W	ENF	1850	−3.2	520	*Goulden et al.* [2011]
	CA-NS2	55.906°N 98.525°W	ENF	1930			
	CA-NS3	55.912°N 98.382°W	ENF	1964			
	CA-NS5	55.863°N 98.485°W	ENF	1981			
	CA-NS6	55.917°N 98.964°W	SRB	1989			
	CA-NS7	56.636°N 99.948°W	SRB	1998			
Alaska (AK)	US-Bn1	63.920°N 145.378°W	ENF	1920	−1.9	300	*Welp et al.* [2007]
	US-Bn2	63.920°N 145.378°W	DBF	1987			
	US-Bn3	63.923°N 145.744°W	SRB	1999			
Saskatchewan (SK)	CA-SF1	54.485 °N 105.818 °W	ENF	1977	0.4	470	*Mkhabela et al.* [2009]
	CA-SF2	54.254 °N 105.878 °W	ENF	1989			
	CA-SF3	54.092 °N 106.005 °W	ENF	1998			
	CA-OJP	53.916 °N, 104.692 °W	ENF	1919			

[a]The annual mean air temperature (T_{air}) and precipitation (P) of each site network is also shown.

MODIS NDVI and FPAR (MOD15) data [*Myneni et al.*, 1997]. A 25 km resolution, Special Sensor Microwave Imager (SSM/I) based global record of daily landscape FT status [*Kim et al.*, 2012] was used to define frozen temperature constraints to the TCF GPP calculations.

[17] The MODIS (MOD13A2) 1 km resolution and 16 day time series VIs (NDVI and EVI) were used as surrogate indicators of vegetation productivity changes over the tower chronosequence sites to evaluate the impact of fire disturbance and vegetation recovery on ecosystem productivity. The 0.5° resolution global annual fire emission database (GFED) [*Giglio et al.*, 2010] was used to define burned area occurrence and BF over the northern domain and the associated redistribution of fire detritus and SOC removal within each 0.5° modeling grid cell. A Palmer Drought Severity Index (PDSI) record derived from National Centers for Environmental Prediction (NCEP) II reanalysis surface meteorology [*Zhao and Running*, 2010] was used to identify large drought events and evaluate their impact on TCF simulations of regional carbon sink activity.

2.3. Model Parameterization

[18] Table 1 presents the general biome properties look-up table (BPLUT) describing biome-specific ecophysiological response characteristics of the TCF model simulations over the northern domain. The biome-specific LUE environmental response parameters, including ε_{mx}, T_{mn_min}, T_{mn_max}, VPD$_{min}$, and VPD$_{max}$, were optimized by matching the probability density function (PDF) and minimizing the root mean square difference (RMSD) between MODIS MOD17 and TCF simulated GPP at 0.5° spatial resolution for the 1 year (2005) model development record. Tower eddy covariance based CO_2 flux data for selected representative land cover types were used for calibrating the TCF soil decomposition model parameters and were independent of the tower sites used for model validation. A Markov Chain Monte Carlo (MCMC) [*Haario et al.*, 2006] approach was used to calibrate selected BPLUT parameters for individual biome types, including optimal soil temperature (T_{opt}) and soil moisture (SM$_{opt}$) levels for soil decomposition, and empirical fitting parameters (a and b) regulating the model soil moisture response. The MCMC calibration was conducted by minimizing the RMSD between site observed and TCF simulated R_{eco}. The calibration tower comparisons indicated

overall favorable algorithm performance (41 sites: R ≥ 0.78; RMSD ≤ 1.50 g C m^{-2} d^{-1}) relative to the tower R_{eco} estimates. However, the calibration results showed generally greater cross-site differences than cross-biome variability in the temperature and moisture response curves; therefore, uniform temperature and moisture response curves were applied to all northern biome types.

[19] The chronosequence tower observation based carbon fluxes were used to determine the plant detritus redistribution (η_1) and SOC consumption (η_2) parameters to adjust the regional TCF simulations from steady state conditions. A prognostic GPP recovery trajectory was first derived for each tower chronosequence from MODIS VI (NDVI and EVI) time series (2000–2010) and corresponding tower GPP observations over the entire vegetation succession period represented by each tower age chronosequence. Specifically, the GPP annual time series were estimated from the growing-season average VI time series of the overlying MODIS 1 km pixels for each chronosequence site based on the ratio of tower GPP to the VI values defined from the mature tower stands. Climate variations should have a large impact on vegetation productivity during later succession when plants may maintain relatively constant foliage cover but show large variations in GPP [*Davis et al.*, 2003; *Knohl et al.*, 2003; *Cook et al.*, 2004; *Desai et al.*, 2005; *Amiro et al.*, 2010]. However, most of the dynamic changes in the ecosystem fluxes and carbon pools occur in the first 10–20 years after fire [*Amiro et al.*, 2010], when changes in photosynthetic canopy cover generally represent the recovery of vegetation productivity [e.g., *Goulden et al.*, 2011]. The TCF model was then run through the entire succession period (>80 years) for each group of chronosequence sites to simulate NEE and SOC recovery using the above prognostic GPP recovery trajectory and site measured surface (<15 cm) soil temperature and moisture data. The η_1 and η_2 parameters were determined by minimizing the difference between TCF simulated and tower observation based annual NEE over the three chronosequences. After fire, 80% (η_1) of NPP was estimated to reallocate to the two fast SOC pools for all three chronosequences; a 20% fire reduction (1 − η_2) in C_{rec} was estimated for the MB and SK chronosequences, while a larger reduction rate (40%) was found for the AK chronosequence, likely due to more SOC accumulated in the upper surface soil layer at the AK sites [*Welp et al.*, 2007].

Table 3. Estimated Uncertainties (1σ) of Selected TCF Parameters[a]

Parameters	Uncertainty (1σ)	Range
T_{mn_max}	2.5°C	[T_{mn_min}, 20°C]
VPD_{max}	500 Pa	[VPD_{min}, 10,000 Pa]
CUE	0.1	[0.2, 0.8]
K_{mx}	0.01 day^{-1}	[0, 0.05 day^{-1}]
T_{opt}	2.5°C	[20°C, 40°C]
SM_{opt}	0.2	[0, 1]
η_1	0.2	[0, 1]
η_2	0.2	[0, 1]

[a]A Monte Carlo approach was used to propagate the parameter uncertainties to estimated carbon fluxes. The parameters follow a normal distribution with mean values defined in Table 1, and the distributions for individual parameters were truncated if the parameter values were out of range (defined in this table).

2.4. Uncertainty Analysis

[20] TCF uncertainty attributed to the model inputs was assessed by comparing NEE outputs against alternative model calculations derived from local tower GPP and meteorology inputs; a Monte Carlo (MC) approach was used to quantify the range in estimated carbon fluxes given uncertainty in key model parameters.

[21] We first conducted three TCF simulations at each tower site using different input data sets to evaluate the impact of uncertainties in GPP and surface meteorology inputs on the NEE estimates. Two model simulation sets driven by tower GPP and MERRA meteorology inputs (NEE_mix) and MODIS NDVI and MERRA inputs (NEE_MERRA), were compared against a benchmark simulation derived from in situ tower GPP, soil temperature, and moisture inputs (NEE_site) to evaluate whether the carbon inputs (i.e., GPP) or surface meteorology were the major uncertainty source for the resulting TCF model NEE estimates. We then used the MC approach to propagate the uncertainties in the post-fire vegetation recovery, fire-induced detritus inputs, and SOC consumption factors through the TCF model to estimate uncertainties in the resulting NEE recovery trajectory at the chronosequence sites. Post-fire vegetation recovery indicated by the EVI or NDVI shows a large dynamic range in the boreal forest [*Beck and Goetz*, 2011], and the post-fire peak EVI values vary by ±20% to account for burn severity and land cover heterogeneity effects at the MODIS spatial resolution (i.e., 1 km). Previous studies show that vegetation carbon use efficiency (CUE) may change during the course of stand development [*Delucia et al.*, 2007; *Goulden et al.*, 2011]; thus, CUE values at the chronosequence sites were set to

0.5 [*Waring et al.*, 1998] with a variable range from 0.2 to 0.8. The SOC consumption rates (η_2) also show a large dynamic range in the boreal region [*Balshi et al.*, 2007], which we assume vary from 0 to 80% in this study. The relative impact of uncertainty in the fire-induced detritus input parameter (η_1) was not evaluated because it has minimal influence on the TCF NEE recovery after the first 1–2 years following a fire event.

[22] The MC approach was also used to estimate spatial patterns of uncertainties in simulated carbon fluxes using best-guess estimates of model parameter uncertainty (Table 3). The parameter uncertainty may be slightly different from the parameter uncertainty defined in the MC simulations at the chronosequence sites. We first conducted a global sensitivity analysis to identify the most sensitive BPLUT parameters affecting TCF derived GPP and NEE fluxes. Model GPP in northern ecosystems was most sensitive to maximum light use efficiency (ε_{mx}), followed by minimum temperature constraints (T_{mn_min} and T_{mn_max}) and VPD_{max}. Estimated NEE was most sensitive to the carbon inputs including GPP and CUE, followed by optimal temperature and moisture conditions (T_{opt} and SM_{opt}) for soil decomposition, and the maximum decomposition rate (K_{mx}). Since the carbon inputs to the SOC pools were proportional to both ε_{mx} and CUE, and since varying ε_{mx} would not affect correlations between GPP and the climate variables, we only analyzed CUE uncertainty impacts on the MC simulations. Uncertainties with normal distributions were defined for each parameter (Table 3), while the distributions for individual parameters were truncated if they exceeded specified ranges. It should be noted that we ignored potential correlations among parameter uncertainties, which may influence resulting simulated carbon flux uncertainties. We performed 1000 model runs, and resulting carbon flux uncertainties were estimated from the standard deviations of the simulation results. For each run, the TCF model was first spun up from prescribed initial conditions to dynamic steady state conditions between simulated NPP and surface SOC stocks under prevailing climate conditions represented by the 11 year (2000–2010) MODIS NDVI and MERRA daily surface meteorology inputs. The GFED defined burned area fractions were then used to adjust the SOC results to nonsteady state conditions following equations (12)–(14).

[23] We used the following approach to assess whether significant correlations between TCF annual GPP estimates and corresponding climate variability indicators (temperature and PDSI) were confirmed beyond the estimated model uncertainty for selected regional subdomains. For

Table 4. Comparison of Modeled Daily GPP (TCF and MOD17) versus Tower Observations at Predominantly Undisturbed Tower Sites ($\geq$45°N)[a]

	Num	RMSD (TCF) (g C m^{-2} d^{-1})	RMSD (MOD17) (g C m^{-2} d^{-1})	Bias (TCF) (%)	Bias (MOD17) (%)	R (TCF)	R (MOD17)
ENF	30	1.94 ± 0.59	1.98 ± 0.65	31.3 ± 21.1	30.5 ± 23.5	0.82 ± 0.15	0.81 ± 0.14
DBF	5	2.29 ± 0.48	3.17 ± 1.00	19.5 ± 7.7	20.0 ± 14.5	0.90 ± 0.04	0.70 ± 0.15
MF	8	1.73 ± 0.42	1.94 ± 0.32	11.1 ± 8.2	17.6 ± 15.0	0.87 ± 0.06	0.84 ± 0.06
SRB	1	0.97 ± 0.0	1.11 ± 0.0	N/A[b]	N/A[b]	0.80 ± 0.0	0.84 ± 0.0
GRS	3	2.03 ± 0.60	1.86 ± 0.33	23.3 ± 9.8	18.8 ± 15.4	0.69 ± 0.27	0.69 ± 0.25

[a]Bias is the absolute difference between modeled and tower-observed annual GPP, normalized by annual means of observed GPP (%). The model GPP results are nonsignificantly different (p > 0.01) from each other, except for DBF areas using the two-tailed *t* test.
[b]The limited tower record length at the SRB site (RU-Cok) was insufficient to determine mean annual GPP and associated bias.
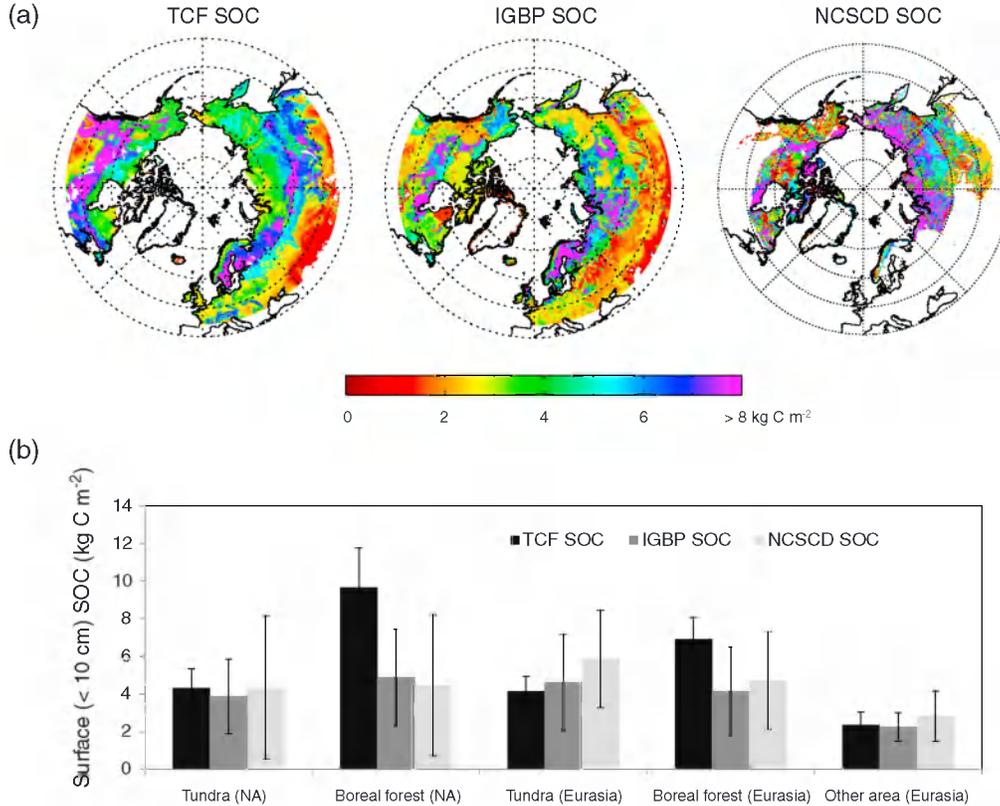
Figure 2. (a) Spatial patterns of estimated surface ($\sim <10$ cm depth) soil organic carbon (SOC, $kg\,C\,m^{-2}$) from TCF simulations and IGBP and NCSCD soil inventory records for the northern domain ($\geq 45°N$); (b) regional mean and standard deviation (indicated by error bar) for tundra, boreal forest, and other regions (mainly grasslands and croplands) of surface SOC for North America (NA) and Eurasia portions of the domain. There were no NCSCD SOC records available for the European portion of the domain at the time of this investigation. A constant (0.2) conversion coefficient was used to estimate surface SOC from the original 1 m depth IGBP and NCSCD SOC data [*Jobbágy and Jackson*, 2000].

temperature, we grouped the regional statistics (mean and standard deviation) of annual GPP from 2000 to 2010 into two subgroups based on growing-season average temperatures (T_{avg}): warm years above multiyear mean T_{avg} and cold years below mean T_{avg}. A one-tailed t test was then used to test whether the GPP mean for classified warm years was significantly larger than the mean for classified cold years. Similarly for PDSI, we grouped the TCF annual GPP statistics into dry years (below multiyear mean PDSI) and wet years (above multiyear mean PDSI) and then tested whether the GPP mean in wet years was significantly larger than the GPP mean in dry years.

3. Results

3.1. Model Validation

3.1.1. GPP

[24] The TCF model GPP simulations were evaluated against daily GPP estimates from independent tower eddy covariance measurements for 47 tower sites representing the major northern biome types (Figure 1a). Overall, model GPP simulations from the NDVI-based LUE algorithm show similar accuracy as the MODIS operational GPP product (MOD17) relative to the tower GPP observations (Figure 1b), and the application of an empirical NDVI-FPAR

relationship does not appear to degrade model GPP accuracy. The TCF LUE algorithm produces favorable GPP results relative to daily tower observations representing a diverse range of northern biomes and climate conditions, with mean correlation $(R) = 0.83$ and $RMSD = 1.93\,g\,C\,m^{-2}\,d^{-1}$ (Table 4) within the documented uncertainty of tower GPP estimates ranging from approximately $1\,g\,C\,m^{-2}\,d^{-1}$ (winter) to $2–4\,g\,C\,m^{-2}\,d^{-1}$ (summer) [*Schaefer et al.*, 2012]. The uncertainty in GPP and R_{eco} partitioning from tower NEE measurements may be even larger in the high latitudes due to large data gaps in eddy covariance CO_2 flux measurements during the dormant season [*Richardson and Hollinger*, 2007]. Additionally, both the TCF and MOD17 GPP products tend to show larger errors in relative high productivity areas, including DBF ($RMSD \geq 2.29\,g\,C\,m^{-2}\,d^{-1}$) sites. The large bias at ENF sites (Table 4) relative to DBF and MF sites is mainly caused by model overestimation of tower GPP at the relatively low productivity ENF sites.

3.1.2. SOC

[25] Two independent inventory based SOC data sets were used for verifying TCF simulated surface ($\sim \leq 10$ cm depth) SOC levels, including the International Geosphere-Biosphere Programme (IGBP) *Global Soil Data Task* [2000] and Northern Circumpolar Soil organic Carbon Database (NCSCD) [*Hugelius et al.*, 2012]. The TCF modeled steady state SOC

Table 5. Correlation Coefficients (R) and Root Mean Square Differences (RMSD) between TCF Modeled Daily Steady State NEE Fluxes and Tower Measurements at Predominantly Undisturbed Sites ($\geq$45°N)[a]

	Num	R Site	RMSD Site (g C m^{-2} d^{-1})	R MERRA	RMSD MERRA (g C m^{-2} d^{-1})	R Mix	RMSD Mix (g C m^{-2} d^{-1})
ENF	15	0.62 ± 0.19	1.39 ± 0.83	0.55 ± 0.20	1.27 ± 0.56	0.66 ± 0.16	1.29 ± 0.72
DBF	3	0.90 ± 0.04	1.92 ± 0.07	0.73 ± 0.09	2.48 ± 0.15	0.92 ± 0.02	2.04 ± 0.16
MF	2	0.72 ± 0.11	1.16 ± 0.39	0.40 ± 0.24	1.49 ± 0.18	0.73 ± 0.11	1.08 ± 0.28
GRS	2	0.75 ± 0.18	1.03 ± 0.16	0.58 ± 0.33	1.36 ± 0.16	0.82 ± 0.13	0.96 ± 0.19

[a]Three groups of TCF simulations were conducted, including simulations derived from site meteorology and tower-measured GPP inputs ("Site"), regional MERRA meteorology and MODIS NDVI inputs ("MERRA"), and MERRA meteorology and tower-measured GPP inputs ("Mix"). A two-tailed t test was used to evaluate the significance of differences in R and RMSD values between different groups of simulations. The test was done for all of the sites as there were not enough samples for individual biome types (except for ENF). The difference between the NEE simulations driven by different GPP inputs (i.e., "Site" versus "MERRA," or "Mix" versus "MERRA") is significant (p < 0.01), while the difference between the two simulations driven by in situ GPP inputs ("Site" versus "Mix") is not.

results for the northern domain show a similar pattern as the IGBP and NCSCD soil inventory data sets for North America (NA) but with notable differences from the IGBP data in Northern Eurasia, especially in tundra areas (Figure 2a). The regional pattern of TCF steady state SOC results is largely determined by the local climate and predominant vegetation type. Areas having higher productivity or with slower soil decomposition rates from colder temperatures tend to accumulate more soil carbon. Therefore, the model results show larger SOC stocks in higher productivity boreal forests of North America (NA) and colder boreal soil areas of northern Siberia. The IGBP data show large soil carbon pools in NA boreal forest, while in northern Eurasia, a large amount of SOC is located in permafrost affected areas and boreal peatlands [*Tarnocai et al.*, 2009]. The regional statistics (Figure 2b) indicate that the model and soil inventory results show similar mean SOC stocks for the major biomes but with larger model SOC estimates for NA boreal forest. Large spatial variability in SOC stocks within tundra and boreal forest areas are also observed in the two inventory data sets. Factors influencing relationships between the TCF and inventory based SOC records include the use of a uniform (0.2) conversion coefficient to estimate surface SOC from 0–1 m depth integrated IGBP and NCSCD inventory data, whereas forests tend to accumulate more carbon in upper soil layers relative to grasslands and shrublands [*Jobbágy and Jackson*, 2000]. Soil texture, microclimate, terrain, and vegetation heterogeneity also influence SOC depth distributions and are not represented by either the TCF model or soil inventory records.

3.1.3. NEE

[26] A summary of correlation (R) and RMSD values between tower and model derived daily NEE fluxes at predominantly undisturbed sites ($\geq$45°N) is presented in Table 5. Overall, TCF simulations derived from tower-observed GPP inputs show stronger correlations (R > 0.6) and lower RMSD (<2 g C m^{-2} d^{-1}) values than results derived from the TCF LUE model based GPP simulations. This indicates that uncertainty in the model GPP calculations accounts for a major portion of uncertainty in the resulting NEE simulations, which is also shown in the comparison of NEE time series at sites representing major regional biome types in Figure 3. The model results generally capture NEE daily variability at
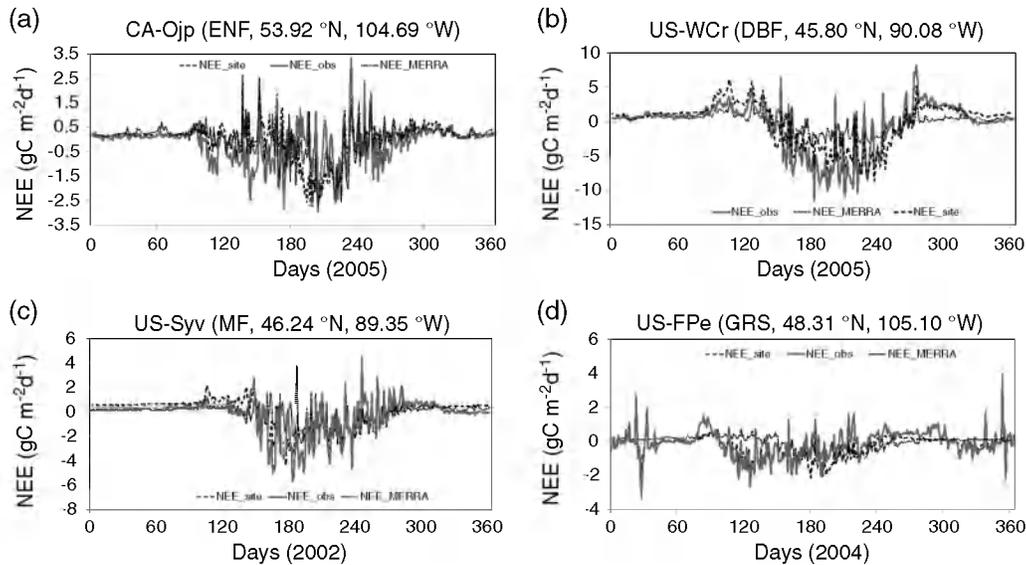

Figure 3. Comparison of seasonal progression of tower and TCF modeled steady state daily NEE fluxes for selected tower sites including (a) an ENF site CA-Ojp, (b) a DBF site US-WCr, (c) a MF site US-Syv, and (d) a GRS site US-FPe. The TCF results include model simulations driven by MERRA meteorology and MODIS NDVI inputs (NEE_MERRA) and tower GPP and meteorology inputs (NEE_site); tower NEE observations are denoted as "NEE_obs."
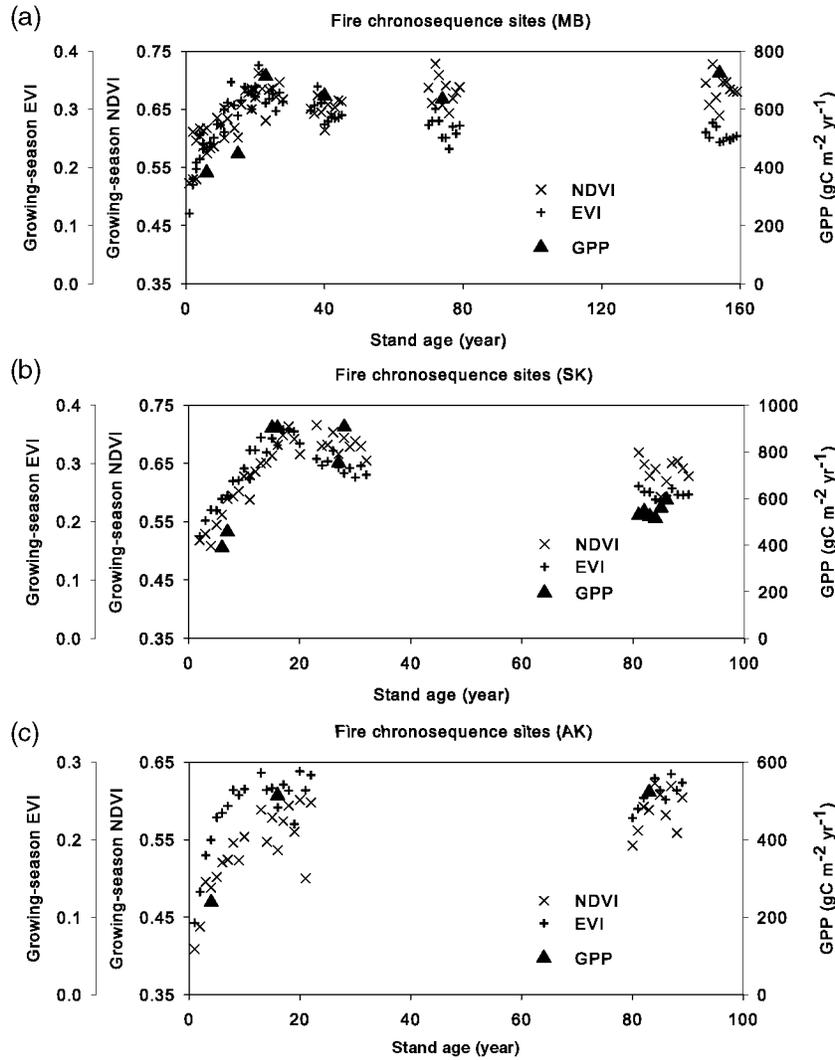
Figure 4. The vegetation recovery trajectory during post-fire succession as represented by tower-observed annual GPP and growing-season average NDVI and EVI values extracted from overlying 1 km MODIS pixels at boreal fire chronosequence sites located in (a) Manitoba (MB), (b) Saskatchewan (SK), and (c) Alaska (AK).

the ENF and MF sites relative to the tower observations, while TCF model NEE accuracy is reduced at the DBF and grassland (GRS) sites primarily due to larger discrepancies between model and tower based GPP estimates. At the DBF site, the model underestimates GPP and does not capture the apparent strong NEE sink activity indicated by the tower data during the peak growing season. At the GRS site, the TCF GPP simulations show inconsistent seasonality relative to tower GPP due to apparent insufficient representation of soil water deficit constraints in the LUE algorithm, which results in shifting seasonality and reduced NEE correspondence. The tower observations also show generally strong NEE sink activity in early summer but weaker sink or source activity later in the growing season, which is not apparent in the TCF simulations driven by MODIS and MERRA inputs. These temporal differences may be caused by neglecting respiration from slowly warming deep soil layers and litterfall seasonality in the TCF simulations. Overall, the TCF results are consistent with the tower observations at the level of tower NEE uncertainty, which has been estimated to be approximately $\pm 30\,g\,C\,m^{-2}\,yr^{-1}$ over accumulated annual

integrals or approximately $\pm 1.6\,g\,C\,m^{-2}\,d^{-1}$ at the daily scale [*Richardson and Hollinger*, 2007].

[27] The MODIS 1 km growing-season average VI (NDVI and EVI) time series generally track post-fire vegetation recovery (R > 0.8) indicated by in situ GPP observations from the three tower chronosequence networks (Figure 4); the TCF nonsteady state NEE simulations based on MODIS VI inputs also generally track observed NEE recovery trends at the chronosequence sites (Figure 5, MB: R = 0.79, RMSD = $60.0\,g\,C\,m^{-2}\,yr^{-1}$; SK: R = 0.71, RMSD = $62.2\,g\,C\,m^{-2}\,yr^{-1}$). These results indicate a large carbon source (positive NEE) during the initial post-fire recovery years due to vegetation canopy and GPP reductions, and enhanced litter decomposition and R_h. The ecosystem shifts to a carbon sink after 5–10 years, with strongest carbon sink activity occurring around 20 years after fire disturbance, due to apparent rapid vegetation canopy recovery indicated by the post-fire MODIS VI and tower GPP records (Figure 4). Our results (Figure 5) also indicate large uncertainties in simulated NEE fluxes during early succession, mainly due to uncertainties in post-fire GPP recovery and
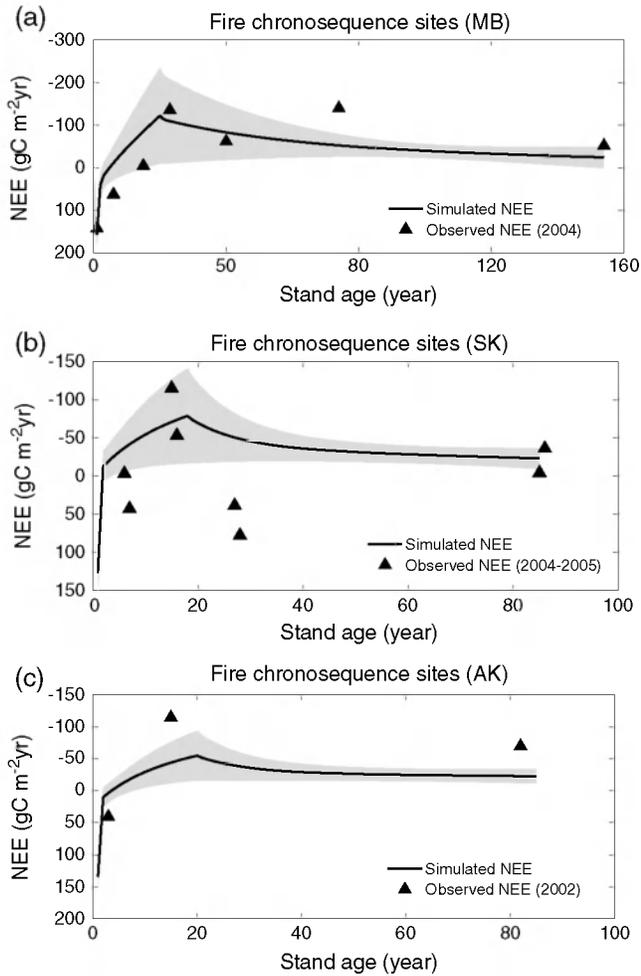
Figure 5. Comparison of tower-observed and model-simulated NEE disturbance recovery trajectories using MODIS EVI time series (2000–2010) at the boreal fire chronosequence sites located in (a) Manitoba (MB), (b) Saskatchewan (SK), and (c) Alaska (AK). The uncertainties (1σ) of model estimated NEE fluxes are shown in gray.

CUE. A general shift from ENF to more productive deciduous species after severe burning in NA boreal forests and fire release of plant available nitrogen (N) promote rapid vegetation recovery, which may be not be well represented by satellite VIs and model assumptions of constant CUE during the course of stand development [*Goulden et al.*, 2011]. The observed carbon sink strength gradually diminishes for older stand ages and may reflect a commensurate decline in vegetation productivity and accumulation of slowly decomposed materials like coarse woody debris. The 1977 SK site has abnormally high ecosystem respiration, which has been attributed to anomalous high decomposition and R_h rates from coarse woody debris [*Mkhabela et al.*, 2009]. There are relatively few measurements available at the AK chronosequence to enable a detailed model-tower comparison over the entire stand age recovery period (Figure 5c); however, the model results are similar to the available AK tower NEE recovery record and consistent with the recovery pattern observed at the other chronosequence sites.

3.2. Response of Regional Carbon Sink Activity to Drought and Fire Events

[28] Regional patterns of TCF simulated GPP anomalies and NEE along with GFED burned area fractions and PDSI results for selected years having large drought or fire events are presented in Figure 6. Large drought and fire events are generally associated with large negative GPP annual anomalies and relatively strong NEE carbon source activity, though the NEE simulations show reduced sensitivity to those events relative to GPP. Documented NA droughts include large events in the early 2000s, especially 2002, while the GPP reduction in areas with severe drought (defined as PDSI < -1) [*Mu et al.*, 2012] accounted for approximately 1.7% of the total estimated GPP (3.34 Pg C yr^{-1}) in NA boreal forests. Two severe summer heat waves impacted Eurasia in the 2000s, including 2003 in Europe and 2010 (not shown) in Russia; the respective GPP drought reduction in these areas accounted for 2.1% and 0.27% of the total estimated GPP (6.12 Pg C yr^{-1}) of the Eurasian boreal forest. The most extensive GFED burning occurs in eastern Siberia DNF areas and grasslands and croplands of western Russia. The two largest fire years in Eurasia burned 1.1% (2003) and 0.8% (2008, not shown) of the Eurasian boreal forest area and reduced regional GPP by 0.55% (33.0 Tg C yr^{-1}) and 0.21% (12.66 Tg C yr^{-1}), respectively. In western Russia, the GFED product indicates extensive burning in croplands and grasslands almost every year since 2001 but with minimal impact to estimated NEE sink/source activity. Instead, annual NEE source activity is more strongly linked with widespread drought in the region, including 2008 and 2010 [*Mu et al.*, 2012]. The GFED data indicate limited burning in NA (<0.5% and 0.7% of respective forest and tundra areas) relative to boreal Eurasia, while the fire-induced NA GPP reduction is also limited (<0.25% or 9.96 Tg C yr^{-1}).

[29] The regional GPP anomalies show overall consistent variations (R ≥ 0.78, p < 0.01, Table 6) with growing-season average air temperature anomalies in NA (including boreal forest and tundra, Figure 7) and Eurasian tundra areas (Figure 8), while mean annual GPP variations in Eurasian boreal forest are more consistent with regional wetting and drying anomalies indicated by the PDSI (R = 0.50, p = 0.06, Table 6). The uncertainty analysis indicates that annual GPP is significantly (p < 0.005) different between relatively warm and cold years in both NA and Eurasian tundra areas despite large uncertainty in the simulations (Figures 7b and 8b). In NA boreal forest, GPP is largely reduced in colder years (e.g., 2000, 2002, 2004, 2008, and 2009), though 2002 was also a severe drought year in western NA. In Eurasian boreal forest, GPP is generally reduced in drought years indicated by lower PDSI values (e.g., 2003, 2006, and 2010), but also in an anomalous cold year (2004). The uncertainty analysis also indicates that annual GPP is significantly (p < 0.001) different beyond model uncertainty between relatively warm and cold years in the NA boreal forest (Figure 7a) and between dry and wet years in the Eurasian boreal forest (Figure 8a). Different responses of NA and Eurasian boreal forest productivity to temperature and drought may be explained by different climate thresholds and species assemblages and associated vegetation responses in these two areas. NA boreal forest
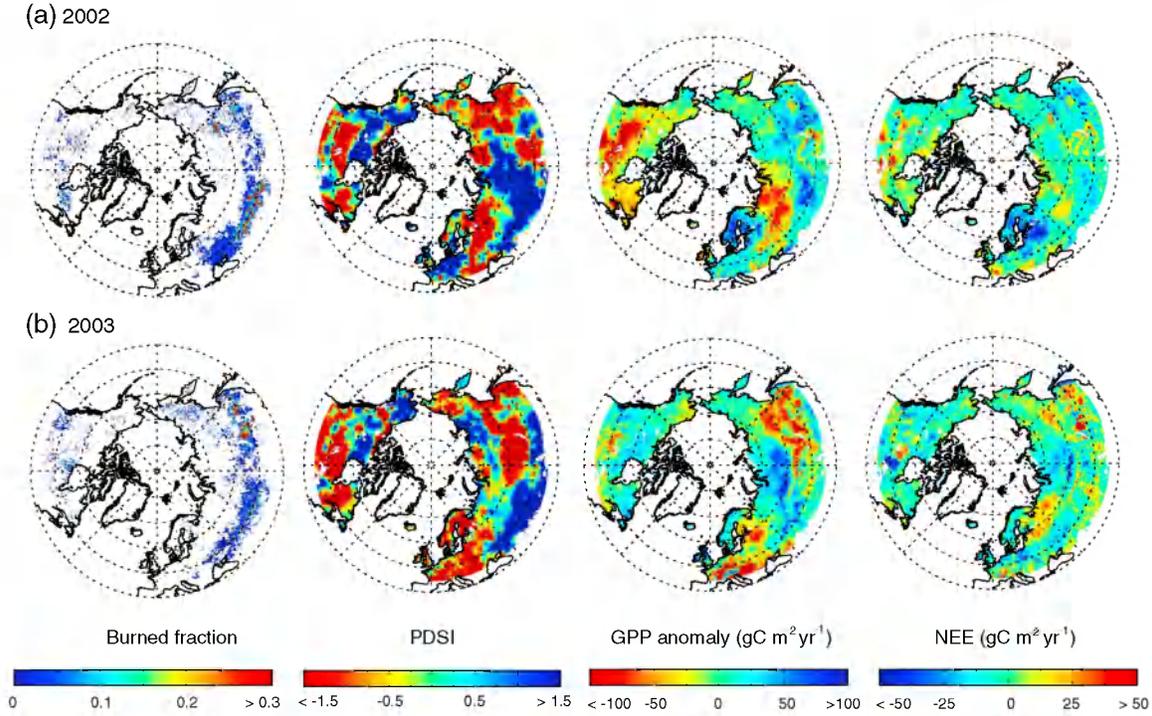
Figure 6. Responses of TCF modeled GPP and NEE to selected large fire and drought events in the 2000s. NA had severe drought in early 2000s; 2003 was a large drought year in Europe and a large fire year in Siberian forest areas. The panels from left to right represent GFED burned area fraction (BF), PDSI, GPP anomaly $(g\,C\,m^{-2}\,yr^{-1})$, and NEE $(g\,C\,m^{-2}\,yr^{-1})$, respectively.

is mainly composed of ENF (73%) and a smaller portion of MF (26%) types. Eurasian boreal forest is more mixed, including ENF (33.5%), DNF (21%), and MF (45%) types, with generally warmer and drier growing seasons (Table 6). The NA boreal forests predominantly show positive productivity responses to warmer temperatures $(R \geq 0.65,\ p < 0.05)$, while only ENF and DNF areas in boreal Eurasia show a general positive productivity response to warmer temperatures $(R \geq 0.59,\ p < 0.05)$ due to lower mean growing-season air temperatures relative to DBF and MF areas (Table 6).

[30] Although generally inversely correlated $(R < -0.6,\ p < 0.05)$ with GPP except in Eurasian tundra areas, the TCF NEE results do not show strong correspondence with either air temperature or drought variability (Table 6). NEE is negatively correlated with growing-season average air temperature in NA boreal forest and tundra areas, with higher correspondence for tundra $(R = -0.66,\ p < 0.05)$, where warmer growing seasons promote apparent carbon sink activity. NEE also shows a positive PDSI drought correlation $(R \geq 0.46,\ p < 0.08)$ in NA boreal forest and tundra, which is likely influenced by strong PDSI and air temperature correspondence. In Eurasian boreal forest and tundra areas, NEE does not show obvious correspondence $(R < 0.2)$ with either air temperature or PDSI variability. Soil heterotrophic respiration shows a temporal lag response to climate variability relative to GPP, while autotrophic respiration covaries with vegetation productivity; this effectively reduces the residual NEE sensitivity to climate variations relative to the larger component carbon fluxes from GPP and R_{eco}.

Table 6. Correlation Coefficients (R) of Regional Mean Modeled GPP/NEE Time Series (2000–2010) versus Growing-Season Average Air Temperature (T_{avg}) and PDSI for NA and Eurasian Boreal Forest and Tundra Areas and Also for the Major Forest Types in Both Domains[a]

	Mean T_{avg} (°C)		Mean P (mm)		R (GPP versus PDSI)		R (GPP versus T_{avg})		R (NEE versus PDSI)		R (NEE versus T_{avg})	
	NA	Eurasia	NA	Eurasia	NA	Eurasia	NA	Eurasia	NA	Eurasia	NA	Eurasia
ENF	12.7	13.3	321	301	−0.084	−0.30	0.69**	0.63**	0.39	−0.01	−0.24	0.13
DNF	N/A	13.0	N/A	282	N/A	0.44	N/A	0.59**	N/A	−0.04	N/A	0.12
DBF	13.6	14.4	551	548	−0.32	0.31	0.65**	−0.27	0.01	0.34	0.20	0.12
MF	13.4	13.4	449	368	−0.48	0.65**	0.89*	−0.01	0.41	−0.34	−0.40	0.30
Forest	12.9	13.3	356	328	−0.18	0.50	0.78*	0.25	0.46	−0.21	−0.30	0.10
Tundra	10.4	10.5	254	248	−0.27	−0.40	0.79*	0.84*	0.49	0.18	−0.66**	0.17

[a]Mean growing-season air temperature (T_{avg}) and precipitation (P) for each biome type are also given.
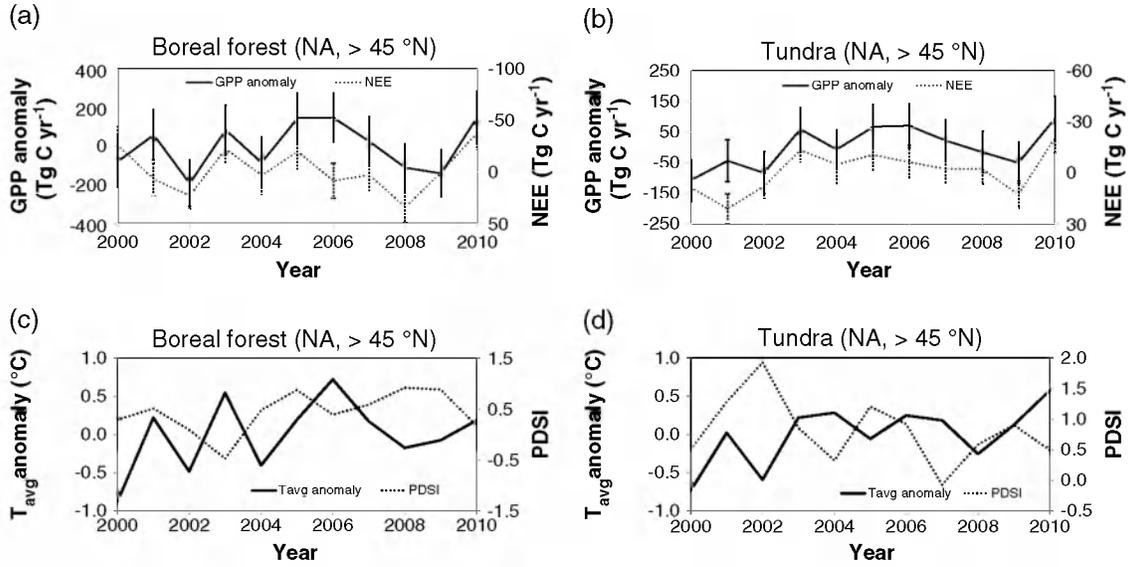*p < 0.01
**p < 0.05

Figure 7. Regional mean time series (2000 to 2010) of (a and b) modeled annual GPP anomalies and NEE, and (c and d) MERRA mean growing-season average air temperature anomalies and PDSI for NA boreal forest and tundra areas of the northern modeling domain. The uncertainties (1σ) of estimated GPP and NEE fluxes are also shown. The regional GPP in warm years is significantly ($p < 0.001$) larger than GPP in cold years for both NA boreal forest and tundra areas using a one-tailed t test, while there is no significant GPP difference ($p > 0.1$) between wet and dry years for both domains.

4. Discussion

4.1. Regional Climate Variation and Fire Impact

[31] Our results show a significant difference in annual GPP between relative warm and cold years over most of the study domain (Figures 7 and 8); our results also show an overall small GPP reduction due to fire relative to larger drought-induced GPP losses (section 3.2). These results indicate that low growing-season temperatures are still a major limiting factor for vegetation productivity in the high latitudes over the study period despite the continued relaxation of regional cold temperature constraints to plant growth and likely increasing carbon losses from large drought and fire events under current warming trends. Previous studies indicate that northern ecosystems are predominantly cold temperature limited [*Yi et al.*, 2010b], while the boreal forest
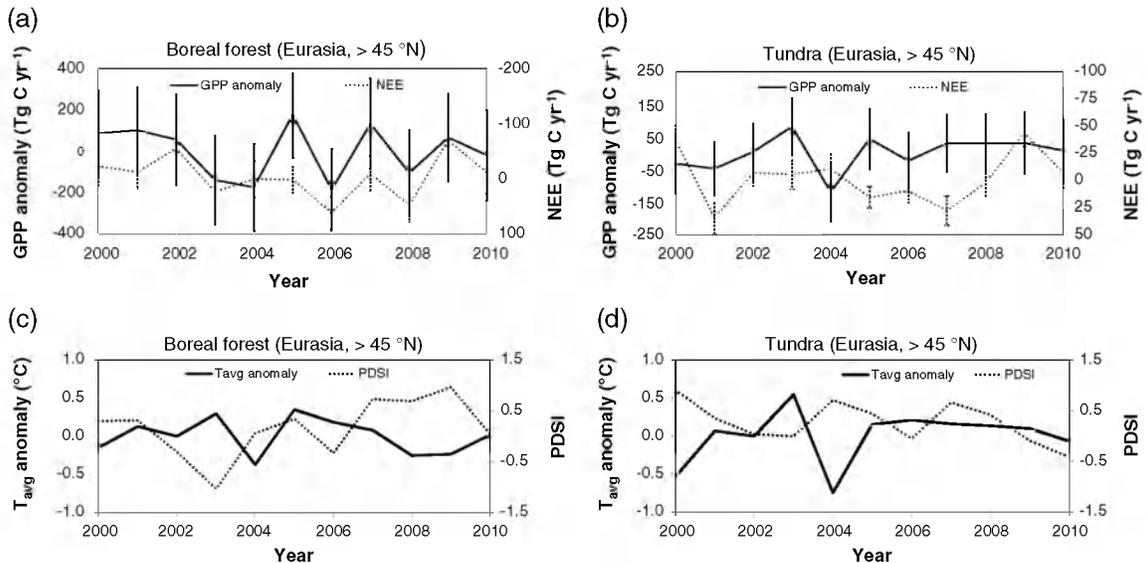

Figure 8. Same as Figure 7, but for the Eurasian portion of the modeling domain. In the Eurasian boreal forest, the regional GPP in wet years is significantly ($p < 0.001$) larger than GPP in dry years, while there was no significant ($p > 0.1$) GPP difference between warm and cold years. In the tundra areas, the regional GPP in warmer years is significantly ($p < 0.005$) larger than GPP in cold years.

13

is becoming increasingly constrained by temperature-induced drought stress [*Zhang et al.*, 2008], with more widespread browning in NA boreal forests than Eurasia [e.g., *Goetz et al.*, 2007; *Beck and Goetz*, 2011]. However, our analysis indicates that the boreal forest productivity response to warming may depend on species type and local climate conditions. Greater sensitivity in Eurasian boreal forest to drying and wetting events than NA boreal forest can be partially explained by regional differences in forest species compositions and climate conditions. A large portion ($\geq$66%) of Eurasian boreal forest, including DNF and MF areas, grows under generally warmer and drier conditions relative to NA boreal forest and is more drought sensitive. Our results also indicate that boreal forests in central and western Canada and interior Alaska have similar drought sensitivity, while boreal forests in eastern Canada and coastal British Columbia have greater precipitation and are relatively more temperature sensitive. These patterns are generally consistent with previous field studies showing that GPP responds differently to climate variations within different plant functional types [*Welp et al.*, 2007], with a positive GPP response to warming in relatively humid areas [*Chen et al.*, 2006; *Peng et al.*, 2011].

[32] Our results also show overall positive correlations between GPP and growing-season temperatures in the high latitudes but no obvious regional correspondence between NEE and temperatures or PDSI (Table 6). This muted model NEE response to climate variability relative to GPP is also consistent with theory and field experiments. Changes in GPP cause similar, compensating soil respiration changes that are largely dependent on photosynthate supply [*Bond-Lamberty et al.*, 2004], while similar GPP and R_{eco} responses to temperature and drought reduce the residual NEE carbon flux response to climate variations [*Baldocchi*, 2008]. Previous studies indicate that GPP and R_{eco} respond positively to spring warming in the middle and high latitudes [*Angert et al.*, 2005; *Chen et al.*, 2006; *Schwalm et al.*, 2010; *Yi et al.*, 2010b] but with variable drought sensitivity depending on substrate conditions, drought severity, and plant functional type [*Ciais et al.*, 2005; *Welp et al.*, 2007; *Schwalm et al.*, 2010; *Schwalm et al.*, 2012].

[33] Our results indicate a relatively small effect of fire disturbance on regional GPP and NEE fluxes in the boreal region compared with larger impacts from drought and temperature variations (section 3.2), while previous studies demonstrate that fire plays a major role in the northern carbon budget [*Balshi et al.*, 2007; *Bond-Lamberty et al.*, 2007; *Hayes et al.*, 2011]. This discrepancy is mainly due to the different carbon fluxes evaluated in these studies. The NEE term represented in this investigation does not include fire emissions, while other studies involving net biome production (NBP) provide a more complete measure of the ecosystem carbon balance that includes carbon emissions from disturbance. The TCF simulations show cumulative annual NEE for the northern domain and 11 year record ranging from 167.1 to -136.6 Tg C yr^{-1}, which is comparable to estimated boreal fire emissions ranging from less than 100 Tg C yr^{-1} to more than 200 Tg C yr^{-1} [*Kasischke et al.*, 2005; *Balshi et al.*, 2007; *Hayes et al.*, 2011]; thus, northern ecosystems can switch from a small carbon sink to a carbon source in large fire years. Moreover, the GFED record indicates that a relatively small portion (<1%) of the boreal

domain burned each year during the post 2000 study period, while a changing fire regime and subsequent shift in vegetation composition will likely play a larger role in future boreal carbon dynamics [*Turetsky et al.*, 2010].

4.2. Uncertainties in Estimated Carbon Fluxes

[34] The model and tower comparisons, and MC simulations both indicate large uncertainties in the TCF carbon flux simulations. Differences between model simulations and tower observations reflect both model and tower observation uncertainty. Uncertainties in tower NEE measurements are generally caused by violations of assumptions, advection in complex topography, and errors in turbulence sampling and measurement, which may range from 30 to 100 g C m^{-2} yr^{-1} [*Richardson and Hollinger*, 2007; *Baldocchi*, 2008]. Partitioning of tower observations into GPP and R_{eco} components is also a source of tower uncertainty that varies with the data processing methods and quality of the NEE measurements [*Reichstein et al.*, 2005]. Tower GPP uncertainty generally increases with GPP magnitude, which can be approximately 2–4 g C m^{-2} d^{-1} during the summer growth period [*Schaefer et al.*, 2012]. Therefore, the TCF carbon fluxes are generally consistent with the tower observations at the level of tower observation uncertainty.

[35] Estimated uncertainties in the TCF carbon flux simulations were primarily attributed to the model inputs, structure, and disturbance recovery treatment. The model comparisons against the tower observations (Table 5) and model uncertainty analysis (section 2.4) indicate that GPP accounts for much of the uncertainty in the TCF NEE simulations due to strong correspondence between GPP and respiration processes (section 3.1.3). The uncertainty in light use efficiency (ε) characterization is a main source of simulated GPP uncertainty. An apparent low model GPP bias in dense canopy areas may reflect MODIS NDVI and FPAR saturation and associated low bias in ε_{mx} [*Turner et al.*, 2006]. Insufficient model VPD representation of soil water deficit constraints on canopy stomatal conductance and ε increases GPP simulation errors under dry conditions [*Leuning et al.*, 2005; *Schaefer et al.*, 2012] (e.g., Figure 3d). The response of ε to diffuse light due to canopy clumping [*Chen et al.*, 2012] and shaded leaf contributions [*Gu et al.*, 2002] to photosynthesis are also not considered in the current GPP model. Other uncertainties associated with the soil decomposition model also contribute to differences between TCF and tower based NEE estimates. The model soil moisture constraint neglects the effects of O$_2$ depletion on soil decomposition in saturated soil and may not adequately represent soil respiration processes in wetland and boreal peatland ecosystems [*Chimner*, 2004]. Neglecting soil respiration from deeper (<10 cm depth) soil layers may cause model R_h bias, especially in permafrost areas [*Harden et al.*, 2012]. The use of an evenly distributed litterfall allocation scheme likely causes seasonal bias in the model R_h estimates, though our investigations show that this bias is small relative to larger uncertainties introduced by the carbon inputs (i.e., GPP).

[36] The boreal chronosequence results indicate large uncertainties in post-fire NEE recovery, especially during early succession (Figure 5), mainly driven by uncertainties in quantifying post-fire vegetation recovery and CUE. The TCF model integrates satellite NDVI-based changes in

photosynthetic canopy cover and other environmental constraints to estimate GPP, which may partially account for fire disturbance impacts on vegetation cover and productivity. However, other post-fire effects including species succession, nutrient cycle, and microclimate changes also affect vegetation recovery and may alter CUE during stand development [*Delucia et al.*, 2007; *Yi et al.*, 2010a; *Goulden et al.*, 2011], which is not considered using a constant CUE term in the TCF simulations. A paucity of boreal chronosequence sites also limits our understanding of how disturbance alters surface litter and soil carbon pools; lack of a long-term regional disturbance history record constrains model representation of the effects of earlier fire disturbance and recovery on the regional carbon cycle.

[37] Part of the above uncertainties associated with model structure and disturbance treatment has been addressed in the parameter uncertainty analysis and the MC simulations (section 2.4). T_{mn_max} and VPD_{max} were used to account for the variation in plant physiological response to atmospheric temperature and moisture conditions. Even though the uncertainty in ε_{mx} was not directly addressed in the MC simulation, the uncertainty in simulated NEE fluxes caused by uncertainty in this parameter was partially addressed by varying CUE due to parameter equifinality. Large uncertainties were assigned to the two disturbance parameters (i.e., η_1 and η_2, Table 3) due to difficulty in accurately determining these two parameters using limited chronosequence tower measurements. The three decomposition parameters (K_{mx}, T_{opt}, and SM_{opt}) were used to account for variations in decomposition rates associated with climate conditions. However, some limitations associated with the model assumptions may not be fully addressed by this analysis. For example, changes in soil environmental conditions after burning and the complex interactions between wildfire, soil thermal and hydrological regimes, and ecosystem carbon dynamics [e.g., *Yi et al.*, 2010a] are not explicitly represented in the TCF model, though future satellite microwave remote sensing retrievals from SMAP may provide useful information on changes in surface soil FT and moisture changes induced by large-scale burning. The fire impact on soil organic carbon pools was generalized using a single response parameter (η_2), while the model does not explicitly represent deeper soil organic layers. Both of these factors limit model capabilities for characterizing the burning of deep soil organic layers and associated impacts on post-fire NEE recovery, which may play an increasing role in the northern carbon cycle due to climate warming [*Mack et al.*, 2011; *Turetsky et al.*, 2010].

[38] Finally, the remote sensing and surface meteorology inputs also contribute to uncertainties in the simulated carbon fluxes but are not directly addressed in the model uncertainty analysis. Large gaps in the MODIS NDVI record in the northern high latitudes [*Beck et al.*, 2006] and the resulting temporal gap filling process introduce uncertainties into the GPP simulations. Previous studies showed strong GPP model sensitivity to surface meteorology inputs, especially surface solar radiation [e.g., *Zhao et al.*, 2006]. A previous study [*Yi et al.*, 2011] indicated large bias in MERRA surface solar radiation, especially in the northern midlatitudes to high latitudes. MERRA also shows a general warm bias in surface daily minimum air temperature, though this is partially considered in the model uncertainty analysis by varying T_{mn_max} (Table 3). Uncertainties also exist in

MERRA soil moisture in the high latitudes [*Yi et al.*, 2011], which may reduce accuracy in the model R_h and NEE calculations, though soil decomposition processes in northern ecosystems are more strongly influenced by cold temperatures rather than low soil moisture conditions on an annual basis. However, the relatively coarse (~0.5°) resolution MERRA data do not represent subgrid scale heterogeneity in surface moisture and temperature conditions and their potential nonlinear effects on R_h in boreal forest and peatlands [*Yi et al.*, 2010a]. An ensemble analysis using multiple meteorology products may help address this uncertainty.

5. Conclusions

[39] Continued warming and changing fire regimes in the northern (≥45°N) latitudes have consequences for land-atmosphere carbon feedbacks to the climate system. The sensitivity of northern ecosystems to annual climate variability, drought, and fire disturbance was investigated using a satellite-based terrestrial carbon flux model. Our results indicate that productivity increases from regional warming still outweigh GPP reductions caused by recent drought stress and fire disturbance from 2000 to 2010 and that these effects exceed apparent uncertainties in both the model and measurements. The NEE response to regional climate variability and fire disturbance is muted due to compensating changes in GPP and respiration, though NEE carbon losses are generally observed in localized areas with severe drought or fire disturbance. Overall, the respective NEE estimated annual carbon source and sink activity for the region ranged from 167 to $-137\,\mathrm{Tg\,C\,yr^{-1}}$; these estimates are similar in magnitude to the direct carbon emissions estimated from regional burning. Thus, a large fire year could effectively cancel out potential NEE carbon sequestration gains, while potential increases in fire disturbance and drought from continued regional warming could offset or exceed potential productivity benefits from lengthening growing seasons.

[40] The model simulations from this investigation are associated with large uncertainties. Model comparisons against tower NEE measurements and the uncertainty analysis indicate that improving model GPP accuracy would lead to the largest improvement in NEE accuracy. Improving the resolution and accuracy of critical inputs would also lead to significant model accuracy gains, including surface meteorological forcings and longer regional burned area records. The results of this investigation are based on a relatively simple satellite-based diagnostic carbon model and 11 year observational record. Longer-term model assessments of the northern carbon cycle response to regional warming trends will require more explicit representation of soil processes, including decomposition and heterotrophic respiration from deeper soil layers, and the effects of permafrost degradation and associated changes in soil moisture and thermal regimes.

[41] The results of this study inform development of a TCF model based carbon (L4_C) product to be produced under the NASA SMAP mission [*Entekhabi et al.*, 2010; *Kimball et al.*, 2012]. First, the TCF results indicate that model performance is generally within the planned product accuracy guidelines (e.g., mean RMSD for NEE ≤30 g C m^{-2} yr^{-1} or 1.6 g C m^{-2} d^{-1}) established in relation

to stand-level carbon flux estimates from sparse tower observation networks. This study also documents initial model development and regional assessment of fire disturbance recovery simulations that may be implemented as an L4_C algorithm option; further algorithm development is needed, however, to extend these results and verify model performance beyond the northern domain of this investigation. Finally, our results indicate that moisture variability and regional drought are a significant environmental constraint to boreal carbon fluxes, even though northern ecosystems are considered primarily energy limited. The L4_C product accuracy will likely benefit from new SMAP-enabled observations of surface soil moisture and temperature variability, including improved (~3–9 km) resolution of associated environmental constraints to model GPP and NEE calculations and surface SOC estimates. This new information will be used to address mission science objectives to quantify NEE in boreal landscapes and improve understanding of terrestrial water, energy, and carbon cycle linkages.

References

Amiro, B. D., et al. (2010), Ecosystem carbon dioxide fluxes after disturbance in forests of North America, *J. Geophys. Res.*, *115*, G00K02, doi:10.1029/2010JG001390.

Angert, A., S. Biraud, C. Bonfils, C. C. Henning, W. Buermann, J. Pinzon, C. J. Tucker, and I. Fung (2005), Drier summers cancel out the CO$_2$ uptake enhancement induced by warmer springs, *Proc. Natl. Acad. Sci. U.S.A.*, *102*, 10,823.

Balshi, M. S., et al. (2007), The role of historical fire disturbance in the carbon dynamics of the pan-boreal region: A process-based analysis, *J. Geophys. Res.*, *112*, G02029, doi:10.1029/2006JG000380.

Baldocchi, D. (2008), Breathing of the terrestrial biosphere: Lessons learned from a global network of carbon dioxide flux measurement systems, *Aust. J. Bot.*, *56*, 1–26.

Beck, P. S., C. Atzberger, K. A. Høgda, B. Johansen, and A. K. Skidmore (2006), Improved monitoring of vegetation dynamics at very high latitudes: A new method using MODIS NDVI, *Remote Sens. Environ.*, *100*, 321–334.

Beck, P. S., and S. J. Goetz (2011), Satellite observations of high northern latitude vegetation productivity changes between 1982 and 2008: Ecological variability and regional differences, *Environ. Res. Lett.*, *6*, 045501.

Bond-Lamberty, B., C. K. Wang, and S. T. Gower (2004), A global relationship between the heterotrophic and autotrophic components of soil respiration?, *Global Change Biol.*, *10*, 1756–1766.

Bond-Lamberty, B., S. D. Peckham, D. E. Ahl, and S. T. Gower (2007), Fire as the dominant driver of central Canadian boreal forest carbon balance, *Nature*, *450*, 89–92.

Chen, J. M., B. Chen, K. Higuchi, J. Liu, D. Chan, D. Worthy, P. Tans, and A. Black (2006), Boreal ecosystems sequestered more carbon in warmer years, *Geophys. Res. Lett.*, *33*, L10803, doi:10.1029/2006GL025919.

Chen, J. M., G. Mo, J. Pisek, J. Liu, F. Deng, M. Ishizawa, and D. Chan (2012), Effects of foliage clumping on the estimation of global terrestrial gross primary productivity, *Global Biogeochem. Cycles*, *26*, GB1019, doi:10.1029/2010GB003996.

Chimner, R. A. (2004), Soil respiration rates of tropical peatlands in Micronesia and Hawaii, *Wetlands*, *24*, 51–56.

Ciais, P., et al. (2005), Europe-wide reduction in primary productivity caused by the heat and drought in 2003, *Nature*, *437*, 529–533.

Cook B. D., et al. (2004), Carbon exchange and venting anomalies in an upland deciduous forest in northern Wisconsin, USA, *Agric. For. Meteorol.*, *126*, 271–295, doi:10.1016/j.agrformet.2004.06.008.

Coursolle, C., et al. (2012), Influence of stand age on the magnitude and seasonality of carbon fluxes in Canadian forests. *Agric. For. Meteorol.*, *165*, 136–148.

Davis, K. J., et al. (2003), The annual cycle of CO$_2$ and H$_2$O exchange over a northern mixed forest as observed from a very tall tower, *Global Change Biol.*, *9*, 1278–1293.

Davidson, E. A., L. V. Verchot, J. H. Cattânio, I. L. Ackerman, and J. E. M. Carvalho (2000), Effects of soil water content on soil respiration in forests and cattle pastures of eastern Amazonia, *Biogeochem.*, *48*(1), 53–69.

DeLucia, E. H., J. E. Drake, R. B. Thomas, and M. Gonzalez-Meler (2007), Forest carbon use efficiency: Is respiration a constant fraction of gross primary production?, *Global Change Biol.*, *13*(6), 1157–1167.

Desai, A. R., P. V. Bolstad, B. D. Cook, K. J. Davis, and E. V. Carey (2005), Comparing net ecosystem exchange of carbon dioxide between an old-growth and mature forest in the upper Midwest, USA, *Agric. For. Meteorol.*, *128*, 33–55, doi:10.1016/j.agrformet.2004.09.005.

Entekhabi, D., et al. (2010), The Soil Moisture Active and Passive (SMAP) Mission, *Proc. IEEE*, *98*(5), 704–716.

Euskirchen, E. S., et al. (2006), Importance of recent shifts in soil thermal dynamics on growing season length, productivity, and carbon sequestration in terrestrial high-latitude ecosystems, *Global Change Biol.*, *12*, 731–750.

Gifford, R. M. (2003), Plant respiration in productivity models: Conceptualization, representation and issues for global terrestrial carbon-cycle research, *Funct. Plant Biol.*, *30*, 171–186.

Giglio, L., J. T. Randerson, G. R. van der Werf, P. S. Kasibhatla, G. J. Collatz, D. C. Morton, and R. S. DeFries (2010), Assessing variability and long-term trends in burned area by merging multiple satellite fire products, *Biogeosci.*, *7*, 1171–1186, doi:10.5194/bg-7-1171-2010.

Global Soil Data Task (2000), Global gridded surfaces of selected soil characteristics (IGBPDIS). International Geosphere-Biosphere Programme—Data and Information Services, Available online [http://www.daac.ornl.gov/] from the ORNL Distributed Active Archive Center, Oak Ridge National Laboratory, Oak Ridge, Tennessee, USA.

Goetz, S. J., M. C. Mack, K. R. Gurney, J. T. Randerson, and R. A. Houghton (2007), Ecosystem responses to recent climate change and fire disturbance at northern high latitudes: Observations and model results contrasting northern Eurasia and North America, *Environ. Res. Lett.*, *2*, 045031, doi:10.1088/1748-9326/2/4/045031.

Goulden, M. L., A. M. S. McMillan, G. C. Winston, A. V. Rocha, K. L. Manies, J. W. Harden, and B. P. Bond-Lamberty (2011), Patterns of NPP, GPP, respiration, and NEP during boreal forest succession, *Global Change Biol.*, *17*, 855–871.

Gu, L., D. Baldocchi, S. B. Verma, T. A. Black, T. Vesala, E. M. Falge, and P. R. Dowty (2002), Advantages of diffuse radiation for terrestrial ecosystem productivity, *J. Geophys. Res.*, *107*, NO. D64050, doi:10.1029/2001JD001242.

Haario, H., M. Laine, A. Mira, and E. Saksman (2006), DRAM: Efficient adaptive MCMC, *Stat. Comput.*, *16*, 339–354.

Harden, J. W., et al. (2012), Field information links permafrost carbon to physical vulnerabilities of thawing, *Geophys. Res. Lett.*, *39*, L15704, doi:10.1029/2012GL051958.

Hayes, D. J., A. D. McGuire, D. W. Kicklighter, K. R. Gurney, T. J. Burnside, and J. M. Melillo (2011), Is the northern high latitude land-based CO$_2$ sink weakening?, *Global Biogeochem. Cycles*, *25*, GB3018, doi:10.1029/2010GB003813.

Heinsch, F. A., et al. (2006), Evaluation of remote sensing based terrestrial productivity from MODIS using regional tower eddy flux network observations, *IEEE Trans. Geosci. Remote Sens.*, *44*(7), 1908–1925, doi:10.1109/TGRS.2005.853936.

Hugelius, G., C. Tarnocai, G. Broll, J. G. Canadell, P. Kuhry, and D. K. Swanson (2012), The Northern Circumpolar Soil Carbon Database: Spatially distributed datasets of soil coverage and soil carbon storage in the northern permafrost regions, *Earth Syst. Sci. Data Discuss.*, *5*, 707–733, doi:10.5194/essdd-5-707-2012.

Ise, T., and P. R. Moorcroft (2006), The global-scale temperature and moisture dependencies of soil organic carbon decomposition: An analysis using a mechanistic decomposition model, *Biogeochem.*, *80*, 217–231.

Jobbágy, E. G., and R. B. Jackson (2000), The vertical distribution of soil organic carbon and its relation to climate and vegetation, *Ecol. Appl.*, *10*(2), 423–436.

Kasischke, E. S., E. J. Hyer, P. C. Novelli, L. P. Bruhwiler, N. H. F. French, A. I. Sukhinin, J. H. Hewson, and B. J. Stocks (2005), Influences of boreal fire emissions on Northern Hemisphere atmospheric carbon and carbon monoxide, *Global Biogeochem. Cycles*, *19*, GB1012, doi:10.1029/2004GB002300.

Kim, Y., J. S. Kimball, K. Zhang, and K. C. McDonald (2012), Satellite detection of increasing Northern Hemisphere non-frozen seasons from 1979 to 2008: Implications for regional vegetation growth, *Remote Sens. Environ.*, *121*, 472–487.

Kimball, J. S., K. C. McDonald, S. W. Running, and S. E. Frolking (2004), Satellite radar remote sensing of seasonal growing seasons for boreal and subalpine evergreen forests, *Remote Sens. Environ.*, *90*, 243–258.

Kimball, J. S., L. A. Jones, K. Zhang, F. A. Heinsch, K. C. McDonald, and W. C. Oechel (2009), A satellite approach to estimate land-atmosphere CO_2 exchange for boreal and arctic biomes using MODIS and AMSR-E, *IEEE Trans. Geosci. Remote Sens.*, *47*, 569–587.

Kimball, J.S., R. Reichle, K.C. McDonald, and P.E. O'Neill (2012), SMAP Algorithm Theoretical Basis Document, Release V.1: L4 Carbon Product. SMAP Project, JPL D-66484, Jet Propulsion Laboratory, Pasadena CA., 73 pp, (http://smap.jpl.nasa.gov/files/smap2/L4_C_InitRel_v1_filt.pdf).

Knohl, A., E. D. Schulze, O. Kolle, N. Buchmann (2003), Large carbon uptake by an unmanaged 250-year-old deciduous forest in Central Germany, *Agric. For. Meteorol.*, *118*, 151–167.

Kurz, W. A., C. C. Dymond, G. Stinson, G. J. Rampley, E. T. Neilson, A. L. Carroll, T. Ebata, and L. Safranyik (2008), Mountain pine beetle and forest carbon feedback to climate change, *Nature*, *452*, 987–990.

Law, B. E., O. J. Sun, J. Campbell, S. Van Tuyl, and P. E. Thornton (2003), Changes in carbon storage and fluxes in a chronosequence of ponderosa pine, *Global Change Biol.*, *9*, 510–524.

Leuning, R., H. A. Cleugh, S. J. Zegelin, and D. Hughes (2005), Carbon and water fluxes over a temperate Eucalyptus forest and a tropical wet/dry savanna in Australia: Measurements and comparison with MODIS remote sensing estimates, *Agric. For. Meteorol.*, *129*, 151–173.

Lloyd, J., and J. A. Taylor (1994), On the temperature dependence of soil respiration, *Funct. Ecol.*, *8*(3), 315–323.

Mack, M. C., et al.(2011), Carbon loss from an unprecedented Arctic tundra wildfire, *Nature*, *475*(7357), 489–492.

McGuire, A. D., et al. (2009), Sensitivity of the carbon cycle in the Arctic to climate change, *Ecol. Monogr.*, *79*(4), 523–555, doi:10.1890/08-2025.1.

Mildrexler, D. J., M. Zhao, F. A. Heinsch, and S. W. Running (2007), A new satellite-based methodology for continental-scale disturbance detection, *Ecolog. Appl.*, *27*(1), 235–550.

Mkhabela, M. S., et al.(2009), Comparison of carbon dynamics and water use efficiency following fire and harvesting in Canadian boreal forests, *Agric. For. Meteorol.*, *149*, 783–794.

Mu, Q., M. Zhao, J. S. Kimball, N. G. McDowell, and S. W. Running (2012), A remotely sensed global terrestrial drought severity index, *Bull. Am. Meteor. Soc.*, doi:10.1175/BAMS-D-11-00213.1.

Myneni, R. B., R. R. Nemani, and S. W. Running (1997), Estimation of global leaf area index and absorbed par using radiative transfer models, *IEEE Trans. Geosci. Remote Sens.*, *35*, 1380–1393.

Nemani, R., C. Keeling, H. Hashimoto, W. Jolly, S. Piper, C. Tucker, R. Myneni, and S. Running (2003), Climate-driven increases in global terrestrial net primary production from 1982 to 1999, *Science*, *300*, 1560–1563.

Peng, C., et al. (2011), A drought-induced pervasive increase in tree mortality across Canada's boreal forests, *Nat. Clim. Change*, *1*, 467–471.

Piao, S., et al. (2008), Net Carbon dioxide losses of northern ecosystems in response to autumn warming, *Nature*, *451*, 49–52.

Potter, C., S. Klooster, R. Myneni, V. Genovese, P. N. Tan, and V. Kumar (2003), Continental-scale comparisons of terrestrial carbon sinks estimated from satellite data and ecosystem modeling 1982–1998, *Global Planet. Change*, *39*, 201–213.

Reichstein, M., et al. (2005), On the separation of net ecosystem exchange into assimilation and ecosystem respiration: Review and improved algorithm, *Global Change Biol.*, *11*, 1424–1439.

Richardson, A. D., and D. Y. Hollinger (2007), A method to estimate the additional uncertainty in gap-filled NEE resulting from long gaps in the CO_2 flux record, *Agric. For. Meteorol.*, *147*, 199–208.

Running, S. W., R. R. Nemani, F. A. Heinsch, M. Zhao, M. Reeves, and H. Hashimoto (2004), A continuous satellite-derived measure of global terrestrial primary production, *Bioscience*, *54*(6), 547–560.

Schaefer, K., et al. (2012), A model-data comparison of gross primary productivity: Results from the North American Carbon Program site synthesis, *J. Geophys. Res.*, *117*, G03010, doi:10.1029/2012JG001960.

Schwalm, C. R., et al. (2010), Assimilation exceeds respiration sensitivity to drought: A FLUXNET synthesis, *Glob. Chang. Biol.*, doi:10.1111/j.1365-2486.2009.01991.x.

Schwalm, C. R., et al. (2012), Reduction in carbon uptake during turn of the century drought in western North America, *Nat. Geosci.*, doi:10.1038/NGEO1529.

Serreze, M. C., and J. A. Francis (2006), The arctic amplification debate, *Clim. Change*, *76*, 241–264.

Tarnocai, C., J. G. Canadell, E. A. G. Schuur, P. Kuhry, G. Mazhitova, and S. Zimov (2009), Soil organic carbon pools in the northern circumpolar permafrost region, *Global Biogeochem. Cycles*, *23*, GB2023, doi:10.1029/2008GB003327.

Thornton, P. E., et al.(2002), Modeling and measuring the effects of disturbance history and climate on carbon and water budgets in evergreen needleleaf forests, *Agric. For. Meteorol.*, *113*,185-222.

Turetsky, M. R., et al. (2010), Recent acceleration of biomass burning and carbon losses in Alaskan forests and peatlands, *Nat. Geosci.*, *4*, 27–31.

Turner, D. P., et al. (2006), Evaluation of MODIS NPP and GPP products across multiple biomes, *Remote Sens. Environ.*, *102*(34), 282–292.

Ulaby, F. T., R. K. Moore, and A. K. Fung (1982), *Microwave Remote Sensing: Active and Passive*, 1064p, Addison-Wesley, Reading, MA.

Waring, R. H., J. J. Landsberg, and M. Williams (1998), Net primary production of forests: A constant fraction of gross primary production? *Tree Physiol.*, *18*, 129–134.

Welp, L. R., J. T. Randerson, and H. P. Liu (2007), The sensitivity of carbon fluxes to spring warming and summer drought depends on plant functional type in boreal forest ecosystems, *Agric. For. Meteorol.*, *147*, 172–185.

White, M. A., P. E. Thornton, S. W. Running, and R. R. Nemani (2000), Parameterization and sensitivity analysis of the Biome-BGC terrestrial ecosystem model: Net primary production controls, *Earth Interact*, *4*.

Yi, S., A. D. McGuire, E. Kasischke, J. Harden, K. Manies, M. Mack, and M. Turetsky (2010a), A dynamic organic soil biogeochemical model for simulating the effects of wildfire on soil environmental conditions and carbon dynamics of black spruce forests, *J Geophys. Res.*, *115*, G04015, doi:10.1029/2010JG001302.

Yi, C., et al. (2010b), Climate control of terrestrial carbon exchange across biomes and continents, *Environ. Res. Lett.*, *5*, 034007, doi:10.1088/1748-9326/5/3/034007.

Yi, Y., J. S. Kimball, L. A. Jones, R. H. Reichle, and K. C. McDonald (2011), Evaluation of MERRA land surface estimates in preparation for the Soil Moisture Active Passive Mission, *J Clim.*, *24*(15), 3797–3816.

Zhang, K., J. S. Kimball, E. H. Hogg, M. Zhao, W. C. Oechel, J. J. Cassano, and S. W. Running (2008), Satellite-based model detection of recent climate-driven changes in northern high-latitude vegetation productivity, *J. Geophys. Res.*, *113*, G03033, doi:10.1029/2007JG000621.

Zhao, M., and S. W. Running (2010), Drought-induced reduction in global terrestrial net primary production from 2000 through 2009, *Science*, *329*, 940–943.

Zhao, M., S. W. Running, and R. R. Nemani (2006), Sensitivity of Moderate Resolution Imaging Spectroradiometer (MODIS) terrestrial primary production to the accuracy of meteorological reanalyses, *J. Geophys. Res.*, *111*, G01002, doi:10.1029/2004JG000004.